Title

Emissions of black carbon, organic, and inorganic aerosols from biomass burning in North America and Asia in 2008

Journal

Journal of Geophysical Research Atmospheres, 116(8)

ISSN

0148-0227

Authors

Kondo, Y
Matsui, H
Moteki, N
et al.

Publication Date

2011

DOI

10.1029/2010JD015152

Emissions of black carbon, organic, and inorganic aerosols from biomass burning in North America and Asia in 2008

Y. Kondo,[1] H. Matsui,[1] N. Moteki,[1] L. Sahu,[1,2] N. Takegawa,[1] M. Kajino,[1,3] Y. Zhao,[4] M. J. Cubison,[5] J. L. Jimenez,[5] S. Vay,[6] G. S. Diskin,[6] B. Anderson,[6] A. Wisthaler,[7] T. Mikoviny,[7] H. E. Fuelberg,[8] D. R. Blake,[9] G. Huey,[10] A. J. Weinheimer,[11] D. J. Knapp,[11] and W. H. Brune[12]

Received 7 October 2010; revised 12 January 2011; accepted 28 January 2011; published 19 April 2011.

[1] Reliable assessment of the impact of aerosols emitted from boreal forest fires on the Arctic climate necessitates improved understanding of emissions and the microphysical properties of carbonaceous (black carbon (BC) and organic aerosols (OA)) and inorganic aerosols. The size distributions of BC were measured by an SP2 based on the laser-induced incandescence technique on board the DC-8 aircraft during the NASA ARCTAS campaign. Aircraft sampling was made in fresh plumes strongly impacted by wildfires in North America (Canada and California) in summer 2008 and in those transported from Asia (Siberia in Russia and Kazakhstan) in spring 2008. We extracted biomass burning plumes using particle and tracer (CO, CH_3CN, and CH_2Cl_2) data. OA constituted the dominant fraction of aerosols mass in the submicron range. The large majority of the emitted particles did not contain BC. We related the combustion phase of the fire as represented by the modified combustion efficiency (MCE) to the emission ratios between BC and other species. In particular, we derived the average emission ratios of BC/CO = 2.3 ± 2.2 and 8.5 ± 5.4 ng m^{-3}/ppbv for BB in North America and Asia, respectively. The difference in the BC/CO emission ratios is likely due to the difference in MCE. The count median diameters and geometric standard deviations of the lognormal size distribution of BC in the BB plumes were 136–141 nm and 1.32–1.36, respectively, and depended little on MCE. These BC particles were thickly coated, with shell/core ratios of 1.3–1.6. These parameters can be used directly for improving model estimates of the impact of BB in the Arctic.

Citation: Kondo, Y., et al. (2011), Emissions of black carbon, organic, and inorganic aerosols from biomass burning in North America and Asia in 2008, *J. Geophys. Res.*, *116*, D08204, doi:10.1029/2010JD015152.

1. Introduction

[2] Boreal forest fires are one of the most important sources of aerosols transported to the Arctic [e.g., *Stohl et al.*, 2006, 2007; *Treffeisen et al.*, 2007; *Eck et al.*, 2009]. Large amounts of aerosols, predominantly in the form of carbonaceous aerosols, namely black carbon (BC) and organic aerosols (OA), are emitted from biomass burning (BB). These particles strongly absorb and scatter solar visible radiation (downwelling and upwelling), influencing the radiation budget in the Arctic. They can also act as cloud condensation nuclei (CCN), which influence the microphysical properties of clouds [*Lubin and Vogelmann*, 2006]. Deposition of BC onto snow and ice changes the surface albedo [*Warren and Wiscombe*, 1980; *Clarke and Noone*, 1985], contributing to warming of the Arctic [*Hansen and Nazarenko*, 2004; *Flanner et al.*, 2007, 2009]. Statistically, Russia and Canada have been the largest sources of BC emitted from boreal forest fires [*Lavoué et al.*, 2000; *Stocks et al.*, 2002; *Conard et al.*, 2002; *Soja et al.*, 2004]. Fire activity may increase in the course of significant warming occurring prominently at high latitudes [*Stocks et al.*, 1998].

[1]Research Center for Advanced Science and Technology, University of Tokyo, Tokyo, Japan.
[2]Now at Physical Research Laboratory, Ahmedabad, India.
[3]Now at Meteorological Research Institute, Tsukuba, Japan.
[4]Air Quality Research Center, University of California, Davis, California, USA.
[5]Department of Chemistry and Biochemistry and CIRES, University of Colorado at Boulder, Boulder, Colorado, USA.
[6]NASA Langley Research Center, Hampton, Virginia, USA.
[7]Institute of Ion Physics and Applied Physics, University of Innsbruck, Innsbruck, Austria.
[8]Department of Meteorology, Florida State University, Tallahassee, Florida, USA.
[9]Department of Chemistry, University of California, Irvine, California, USA.
[10]School of Earth and Atmospheric Sciences, Georgia Institute of Technology, Atlanta, Georgia, USA.
[11]Atmospheric Chemistry Division, National Center for Atmospheric Research, Boulder, Colorado, USA.
[12]Department of Meteorology, Pennsylvania State University, University Park, Pennsylvania, USA.

0148-0227/11/2010JD015152

[3] Reliable estimates of the effects of BC on the climate of the Arctic by global models necessitate quantitative understanding of emissions of BC, aging and removal, and microphysical properties [e.g., *Stier et al.*, 2006; *Textor et al.*, 2006; *Koch et al.*, 2009]. More specifically, calculations of the effects of light absorption by BC require photo-absorption cross sections and size distributions of BC. The cross section depends on diameter, and mixing state, together with the refractive index and shapes of BC [e.g., *Moteki et al.*, 2010; *Moteki and Kondo*, 2010; *Shiraiwa et al.*, 2010]. The size distributions of BC are controlled by emissions, transport, and deposition of BC. The coating of BC by nonrefractory species also influences the CCN activity of BC [e.g., *Riemer et al.*, 2004; *Oshima et al.*, 2009; *Kuwata et al.*, 2009] and thus the efficiency of wet deposition, partly compensating for the amplification of light absorption [*Stier et al.*, 2006]. The effect of BC on global and regional climate is currently poorly represented by models [e.g., *Textor et al.*, 2006; *Koch et al.*, 2009], owing in large part to the lack of constraints on emissions and the evolution of these parameters.

[4] Previous estimates of emission factors of BC are considered to be highly uncertain, because they are based on measurements with large uncertainties [*Reid et al.*, 2005]. In particular, interference by coemitted organic aerosol (OA) can cause large errors in BC measurements by thermal optical transmittance and filter-based absorption photometers [e.g., *Reid et al.*, 2005; *Kondo et al.*, 2009, 2011]. Reliable measurements of BC in the Arctic in the spring of 2008 using a single particle soot photometer (SP2) were reported by *Warneke et al.* [2009, 2010]. They observed transport of enhanced BC emitted from BB in Siberia and Kazakhstan over the Alaskan Arctic together with BC-CO correlations.

[5] There is a critical need to characterize the emission ratios and microphysical properties of BC near BB sources before being transported over long distances. We also need to understand the evolution of the microphysical properties of BC after emission for improved representation of these parameters and processes by models. The major objectives of this study are to elucidate these key parameters and processes of BC using a well-calibrated SP2 based on laser-induced incandescence (LII) [e.g., *Moteki and Kondo*, 2007, 2008; *Schwarz et al.*, 2006, 2008; *Kondo et al.*, 2011].

[6] For this purpose, we made measurements of BC and light-scattering particles (LSP) in the submicron range by the SP2 on board the NASA DC-8 aircraft over Alaska and Canada during the Arctic Research of the Composition of the Troposphere from Aircraft and Satellite (ARCTAS) mission in the spring (ARCTAS-A) and summer (ARCTAS-B) of 2008 [*Jacob et al.*, 2010]. Frequent aircraft samplings were made in plumes from boreal forest fires that occurred in Canada and California in summer and in Asia (Siberia and Kazakhstan) in spring. It is noted that in 2008, the boreal wildfires in southern Siberia and agricultural fires in Kazakhstan both occurred unusually early in spring and were much more intense than usual at that time of year [*Warneke et al.*, 2009].

[7] In Canada, aerosol measurements in large plumes were made in the vicinity of the burning areas 1–2 h after the emissions. We have derived the emission ratios of aerosols from BB based on the measurements with unprecedented accuracy. We sampled emissions from wildfires emitted under varying combustion conditions, namely flaming and smoldering fire phases. We systematically interpret the dependence of the emission ratios on the conditions of combustion.

[8] The air masses impacted by BB in Asia were sampled 2–3 days after the emissions. We identified the locations of fires that influenced concentrations of BC by using kinematic back trajectories. We selected data little influenced by wet deposition during transport to estimate the emission ratios. These observations have enabled detailed comparisons of the aerosol emission ratios and their microphysical properties in the two regions.

[9] The most important parameters and processes presented by this study are the evolution of the size distributions and mixing state (coating thickness) of BC, the emission ratios of BC versus CO and CO_2, and their dependence on the conditions of combustion. We have also elucidated the difference of these parameters between the BB plumes from Asia and North America, which are the two major regions of boreal forest fires. These parameters can be used directly for improving model estimates of the impact of BB on climate, especially in the Arctic.

2. Aircraft Observations and Methodology of Data Analysis

2.1. Instrumentation

[10] The data used for this study are the mass, volume, and number concentrations of BC and LSP, mixing ratios of carbon dioxide (CO_2), carbon monoxide (CO), acetonitrile (CH_3CN), dichloromethane (CH_2Cl_2), sulfur dioxide (SO_2), dimethyl sulfide (DMS), and reactive nitrogen (NO_x, NO_y, PANs, and HNO_3), and submicron aerosol chemical composition. The instruments used for the present study and their measurement accuracies are summarized in Table 1, together with their references.

[11] The number concentrations of BC and LSP and the mixing state of BC (coating thickness of BC by nonrefractory components) were measured by the SP2. The measurement principle and schematic diagram of the SP2 have been described previously [*Gao et al.*, 2007; *Moteki and Kondo*, 2007], and detailed descriptions of the calibration of the SP2 used for ARCTAS are given elsewhere [*Moteki and Kondo*, 2010; *Kondo et al.*, 2011]. We summarize the important points below.

[12] Each BC particle sampled by the SP2 was irradiated by a laser beam at a wavelength of 1064 nm and thus heated to incandescence. The SP2 monitors LII signals in two distinct visible bands (λ = 300–550 nm and 580–710 nm). In addition, laser light scattered by individual particles was detected by two avalanche photodiodes to measure the sizes and number concentrations of LSP.

[13] BC particles can be identified by the ratio of LII intensities of the two visible bands, because the ratio is a proxy for the vaporization temperature of the particles. The vaporization temperature of ambient BC was measured to be about 4000 K [*Schwarz et al.*, 2006]. The BC mass for each particle (m_{SP2}) was estimated from the LII peak intensity. We measured the LII peak intensities of monodisperse BC aerosols that were mass selected by an aerosol particle mass analyzer (APM; Model-302, KANOMAX, Inc., Japan) with a 400°C heated inlet [*Moteki and Kondo*, 2007]. BC in

Table 1. Measurements During ARCTAS

	Measurement Technique	Accuracy	References
BC	SP2	±10%	*Moteki and Kondo* [2007, 2010]
LSP number distribution	SP2	±10%	*Moteki and Kondo* [2007, 2010]
LSP volume distribution[a]	SP2	±30%	
Aerosol chemistry	AMS	±35%	*DeCarlo et al.* [2006, 2008] and *Dunlea et al.* [2009]
CO	TDLAS	±2%	*Sachse et al.* [1987]
CO_2	NDIR gas analyzer	±0.25 ppmv	*Vay et al.* [2003]
CH_3CN	PTR-MS	±10%	*Wisthaler et al.* [2002]
CH_2Cl_2	WAS-GC	–	*Blake et al.* [2003]
DMS	WAS-GC	–	*Blake et al.* [2003]
SO_2 (CIT)	CIMS	±(50% of measurement value + 100 pptv)	*Crounse et al.* [2006, 2009]
SO_2 (GIT)	CIMS	–	*Slusher et al.* [2004] and *Kim et al.* [2007]
NO_x and NO_y	Chemiluminescence	±10% and ±15%	*Weinheimer et al.* [1994]
PANs	CIMS		*Slusher et al.* [2004] and *Kim et al.* [2007]
HNO_3	CIMS		*Crounse et al.* [2006, 2009]
OH	LIF	±40%	*Brune et al.* [1999]

[a]Estimated by uncertainty propagation from the number distribution.

ambient air was extracted by vaporization of the condensed compounds coating the BC particles by means of the heated inlet. The SP2 calibration using ambient BC was made for several hours on 10 November 2009. The error in extracting refractory BC mass is estimated to be less than about 10% [*Kondo et al.*, 2011]. This extraction procedure means that the definition of the mass of ambient BC is the mass of incandescent aerosols refractory at 400°C (m_{ref}*). The uncertainty of m_{ref}* is about 10%.

[14] The LII peak intensity increased linearly with mass up to about 20 femtograms (fg). At higher mass, the relationships deviated from linearity. We used the LII peak intensity– m_{ref}* relationship for ambient BC to derive the BC size distributions. In this way, m_{SP2} is fully traceable to the calibration standards (m_{ref}*).

[15] The mass equivalent diameters of the BC cores (D_{BC}) were calculated by assuming a density (ρ_{BC}) of 2 g cm^{-3}, which is also close to the value of 1.77 g cm^{-3} derived by *Park et al.* [2004]. About 10% uncertainty in ρ_{BC} led to errors of a few % in D_{BC}. The D_{BC} detection range of the SP2 used for this study was 80–860 nm. The absolute accuracy of the measurements of mass concentration of BC is estimated to be about 10% [*Kondo et al.*, 2011].

[16] The diameters of the coated BC particles (shell diameters, D_p) were derived using the scattering signals for D_p. The coating thickness of BC or shell/core ratio (D_p/D_{BC} ratio) is a useful conceptual parameter to represent the mixing state of BC. A detailed description of the method to derive D_p is given by *Kondo et al.* [2011].

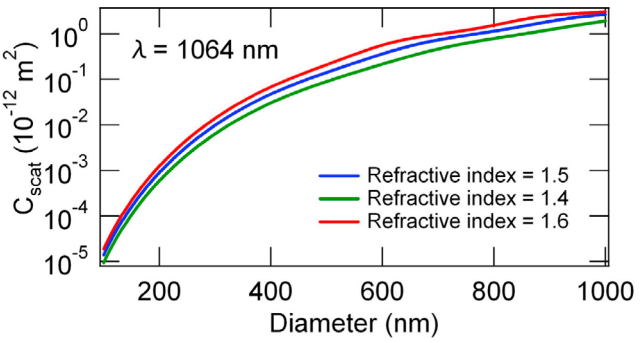

Figure 1. Calculated scattering cross sections as a function of particle diameter for different refractive indices at a wavelength of 1064 nm.

[17] LSP scatters laser light but does not incandesce. The peak scattering signal was converted to the scattering cross section of the particles. Calibration was made first by using polystyrene latex (PSL) particles with a refractive index of 1.59 + 0i. The calibration curve of PSL converts to that of $(NH_4)_2SO_4$ with a refractive index of 1.52 + 0i based on the Mie theory algorithm developed by *Bohren and Huffman* [1998]. The diameters of LSP (D_p) were estimated from this curve with an uncertainty of about 10% in the size range of about 200–750 nm [*Moteki and Kondo*, 2008]. We used $(NH_4)_2SO_4$ in defining D_p because it generally constitutes an important fraction of PM_1 and its refractive index is well known. Refractive indices of a number of OA were reported to range between 1.50 and 1.63 by *Jacobson* [1999]. Refractive indices of OA emitted by BB were measured to be in the range of about 1.56–1.64 at visible wavelengths [*Levin et al.*, 2010]. Refractive indices of SOA photochemically generated from α- and β-pinene and toluene were measured to range from 1.4 to 1.5 at λ = 670 nm [*Kim et al.*, 2010].

[18] Figure 1 shows the calculated scattering cross sections of particles with refractive indices of 1.5 ± 0.1 at a wavelength of 1064 nm based on Mie theory. The changes in particle diameters for changes in the refractive index of ±0.1 from 1.5 + 0i for the same scattering cross sections in the diameter range of 200–500 nm is within 10%, as summarized in Table 2. The uncertainty in D_p by possible changes in the refractive indices of LSP is estimated to be about 10%

Table 2. Comparison of Particle Diameter D_p (N) in Units of nm Estimated for Different Refractive Indices (N) and Their Ratios

D_p(1.5)	D_p(1.4)	D_p(1.6)	D_p(1.4)/D_p(1.5)	D_p(1.6)/D_p(1.5)
200	214	189	1.070	0.945
250	269	236	1.076	0.944
300	324	283	1.080	0.943
350	380	328	1.086	0.937
400	437	374	1.093	0.935
450	494	418	1.098	0.929
500	551	463	1.102	0.926

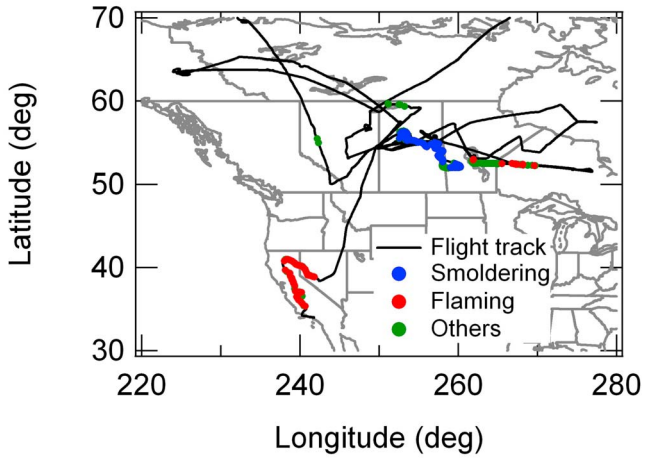

Figure 2. Flight track of the DC-8 over Canada during ARCTAS-B. Phases of BB of the air masses sampled are shown with circles.

considering the reported refractive indices of inorganic and organic aerosols. The total mass concentrations of BC (M_{BC}) and volume concentrations of LSP (V_{SC}) were derived by integrating the size distributions with respect to diameter. The propagated uncertainty of V_{SC} from the uncertainty of D_p is estimated to be about 30%. We did not convert V_{SC} to the mass concentration of LSP because the densities of LSP are not provided by the SP2 measurements. The values of M_{BC} and V_{SC} are given in the units of mass and volume per unit volume of air at standard temperature and pressure (STP; 273.15 K and 1013 hPa), respectively.

[19] Sample air was provided to the instruments using a forward facing, window-mounted inlet probe. Real-time measurements of air speed, static pressure, and temperature were used to maintain isokinetic flow through the inlet tip to minimize inertial enhancement or depletion of coarse particles. Detailed measurements made during the DC-8 Inlet Characterization Experiment (DICE) in the spring of 2003 showed that the inlet efficiently transmits both dust and sea salt particles smaller than 4 μm in dry diameter [*McNaughton et al.*, 2007].

2.2. Air Sampling of Fire Plumes

[20] Figure 2 shows the flight tracks of the NASA DC-8 aircraft, flown from Cold Lake (54°N, 110°W), Alberta, Canada, between 29 June and 10 July 2008, and the transit flight to Palmdale, CA on 13 July. On 29 June, 102 fires were burning and more than half of those ignitions resulted from lightning strikes that occurred within the previous 24 h (A. J. Soja et al., ARCTAS: The perfect smoke, in *The Canadian Smoke Newsletter*, pp. 2–7, Fall 2008). Most of the plumes were encountered over Saskatchewan Province, while some of them were measured over the Yukon Territory and Manitoba. A substantial portion of the flight time was devoted to sampling forest fire plumes within a few hours after emission mostly in the boundary layer (BL) and the lower free troposphere (FT). Figure 2 shows the locations of the sampling of the BB plumes used for the present study that includes data obtained in forest fire plumes in California during the transit flight.

[21] Large-scale BB occurred in Siberia (boreal forest fires) in Russia and in Kazakhstan (agricultural fires) in March and April 2008 [*Warneke et al.*, 2009, 2010]. The air masses impacted by these fires were transported from these regions and were sampled by the local flights from Fairbanks, Alaska, in April 2008 during ARCTAS-A. The flight tracks of the DC-8 during ARCTAS-A are shown by *Jacob et al.* [2010]. These data are used for comparison with the ARCTAS-B data.

[22] Satellite-derived column amounts of CO from the Measurements of Pollution in the Troposphere (MOPITT) instrument [*Drummond and Mand*, 1996; *Bowman*, 2006] and aerosol optical depth (AOD) from the Moderate resolution Imaging Spectroradiometer (MODIS) [*Remer et al.*, 2005] during ARCTAS-A were similar to monthly averages for individual months over the Alaskan Arctic (the region including both measurements and transport pathways of measured air parcels) [*Matsui et al.*, 2011]. This suggests that ARCTAS-A data are representative of the North American Arctic in April 2008.

[23] Air masses impacted by forest fires that occurred in California were also sampled by the DC-8 ARCTAS instrument payload on 18–24 June 2008 for the California Air Resources Board (CARB) [*Singh et al.*, 2010]. We used relevant data obtained during ARCTAS-CARB for comparison with the ARCTAS-B data.

2.3. Backward Trajectories

[24] We used 10 day backward trajectories calculated every minute along the flight tracks using a kinematic model [*Fuelberg et al.*, 2010, and references therein]. The meteorological data were from runs of the Weather Research and Forecasting (WRF) model with a horizontal resolution of 45 km and 50 vertical layers [*Skamarock et al.*, 2008]. Source regions were identified as the regions (projected onto the surface) where the backward trajectories encountered and remained in altitudes below 700 hPa (about 3 km above sea level), which is the approximate altitude of the upper boundary of the BL over the land during daytime.

[25] Air masses with origins outside Canada were excluded for the analysis of the ARCTAS-B data, which focuses on near-field emissions. Some of the air masses sampled during ARCTAS-A were estimated to have originated from two different biomass burning regions in Asia from 10 day back trajectories.

[26] We calculated the accumulated precipitation along each trajectory (APT) using Global Precipitation Climatology Project (GPCP) global precipitation data [*Huffman et al.*, 2001; *Adler et al.*, 2003]. We used daily data (version 1.1) with a horizontal resolution of 1 × 1 degree. The GPCP data were derived solely from observations based on gauge measurements and estimates of rainfall by geostationary and polar orbiting satellites. Precipitation at the surface (i.e., vertically integrated) was summed up along the trajectories from the sampling location to the identified source regions. We used the APT data as a measure of wet removal of water-soluble species during transport. The uncertainties in the estimates of source regions and APT were calculated by using two meteorological data sets for trajectory calculations and three precipitation data sets, including the GPCP data. The comparison has shown that the general features of the statistics and conclusions obtained in this study do

not change with the choice of trajectory model and meteorological and precipitation data sets. More detailed descriptions of the uncertainties in the estimation of the source regions and APT are given elsewhere [*Matsui et al.*, 2011].

2.4. Extraction of Fire Plumes

[27] We first determined species background concentrations to quantify the effect of BB on the concentrations of the species measured on board the aircraft. They were determined as the 5th percentiles of the values in every 10 K range of potential temperature, and they were linearly interpolated vertically. The background values of most of the species were close to zero, except for CO_2 and CO. The differences between the measured and background concentrations (Δ values) were used for the analysis. The 1 min averaged data with $\Delta CO > 20$ parts per billion by volume (ppbv) were used for the statistical analysis to obtain emission ratios from individual data points with sufficient precision maintaining a sufficient number of the data points for statistical analysis.

[28] We selected data strongly influenced by BB using the concentrations of trace hydrocarbon species, CH_3CN and CH_2Cl_2, as described in detail by *Matsui et al.* [2011]. CH_3CN is known to be emitted from forest fires [*de Gouw et al.*, 2003]. CH_2Cl_2 is emitted from industrial solvents, but not emitted from combustion of fossil fuels [*Chen et al.*, 2007; *Choi et al.*, 2003]. However, it can be used as a tracer of anthropogenic emissions of aerosols because the emissions of solvent (CH_2Cl_2) generally coexist with emissions of species by fossil fuel combustion. The BB-impacted air masses transported from Asia were defined as those with $\Delta CH_3CN > 50$ parts per trillion by volume (pptv) and $\Delta CH_2Cl_2 < 5 - 10$ pptv. The threshold of ΔCH_2Cl_2 increased from 5 pptv at $\Delta CH_3CN = 50$ pptv to 10 pptv at $\Delta CH_3CN > 100$ pptv, as depicted in Figure 3 of *Matsui et al.* [2011]. For the Canadian BB, the data selection was made using the thresholds of $\Delta CH_3CN > 100$ pptv and $\Delta CH_2Cl_2 < 10$ pptv.

2.5. Modified Combustion Efficiency

[29] The phase of BB has been shown to be represented by the combustion efficiency (CE) or modified combustion efficiency (MCE) [e.g., *Delmas et al.*, 1995; *Yokelson et al.*, 1999, 2008]. The calculation of CE requires measurement of incompletely oxidized compounds (CO) and reduced compounds such as methane, nonmethane hydrocarbons, and ammonia, among others [*Ward et al.*, 1991], while MCE is estimated only from the $\Delta CO/\Delta CO_2$ ratio.

$$MCE = \Delta CO_2/(\Delta CO_2 + \Delta CO) = 1/(1 + \Delta CO/\Delta CO_2). \quad (1)$$

MCE is useful in interpreting observed emission ratios as a function of MCE, irrespective of the relative amount of data in different combustion phases [*Yokelson et al.*, 1999; *Goode et al.*, 2000]. A MCE of 0.9 is sometimes treated as the value classifying air masses predominantly influenced by combustion in the flaming phase (MCE > 0.9) whereas, MCE < 0.9 represents the smoldering phase [*Reid et al.*, 2005]. The 1 s time resolution of CO and CO_2 data led to the correspondingly high time resolution of the MCE values. This parameter was used for the interpretation of the data impacted by BB.

3. Aerosols in BB Plumes in Canada and California During ARCTAS-B

[30] In Figure 3 (top), we show the time periods of sampling BB plumes identified by the methods discussed in sections 2.3 and 2.4. Figures 3 (top) and 3 (middle) show the time series plots of CO, M_{BC}, V_{SC}, MCE, and NO_x/NO_y ratio measured during Flight 18 (F#18) on 1 July. The APT and altitude of the DC-8 are shown in Figure 3 (bottom). The M_{BC} and V_{SC} values were greatly enhanced during encounters of wildfire plumes. In Figures 3 (top) and 3 (bottom), we show the time periods of sampling BB plumes identified by the methods discussed in sections 2.3 and 2.4. Generally, the MCE was lower than 0.95 in the relatively fresh plumes ($NO_x/NO_y > 0.4$) sampled during this flight.

[31] Figure 4 shows the $\Delta M_{BC}/\Delta CO$ correlation versus the estimated APT that the air masses experienced within 24 h prior to sampling. The integration time in calculating the APT was fixed at 24 h, independent of the age of the BB plumes. Most of the Canadian and Californian air masses experienced little precipitation (APT < 3 mm). For the analysis of the ARCTAS-B and CARB data, we selected data with APT < 1 mm to minimize the effect of wet deposition on the analysis of aerosols.

[32] The first panel in Figure 5 (left) shows the ΔCO-ΔCO_2 correlations used to derive the MCE for individual plumes. Depending on the $\Delta CO/\Delta CO_2$ ratios, the phases of combustion of these plumes were classified as smoldering, flaming, and others. It should be noted that the Δ values were used for the statistical analysis throughout this study, and the linear regressions are used only for supplementary analysis. The locations of the measurements of the plumes with the different combustion phases are shown in Figure 2. Smoldering phase plumes were measured mainly on 1 July during F#18 (Figure 3), and flaming phase plumes were measured on 4 July (F#19) and 13 July (F#24 in California). The flaming phase data obtained in California are shown with crosses. No smoldering phase data were obtained in California during ARCTAS-B. The correlations of the flaming phase data measured in Canada and California showed no statistical differences, as discussed below. Considering this, the data obtained in these regions were grouped as North American for statistical analysis. Figure 6 shows the profiles of M_{BC} and V_{SC} measured over North America during ARCTAS-B. The data points are color coded by the phase of BB. The color-coded data are also with APT < 1 mm.

[33] Figure 7 shows the average number and mass (or volume) size distributions of BC and LSP observed in layers impacted by wildfires over North America. A small discontinuity in the BC mass size distributions near 200 nm is a numerical artifact in constructing the size distributions from the data in each size bin. The count median diameters (CMD) of the lognormal fitted BC size distributions were unvarying at 136 ± 6 nm, with a geometric standard deviation (σ_{gc}) of 1.32, although the CMD slightly increased with the increase in MCE, as discussed in section 8. The size distributions of the LSP were also unvarying, and their

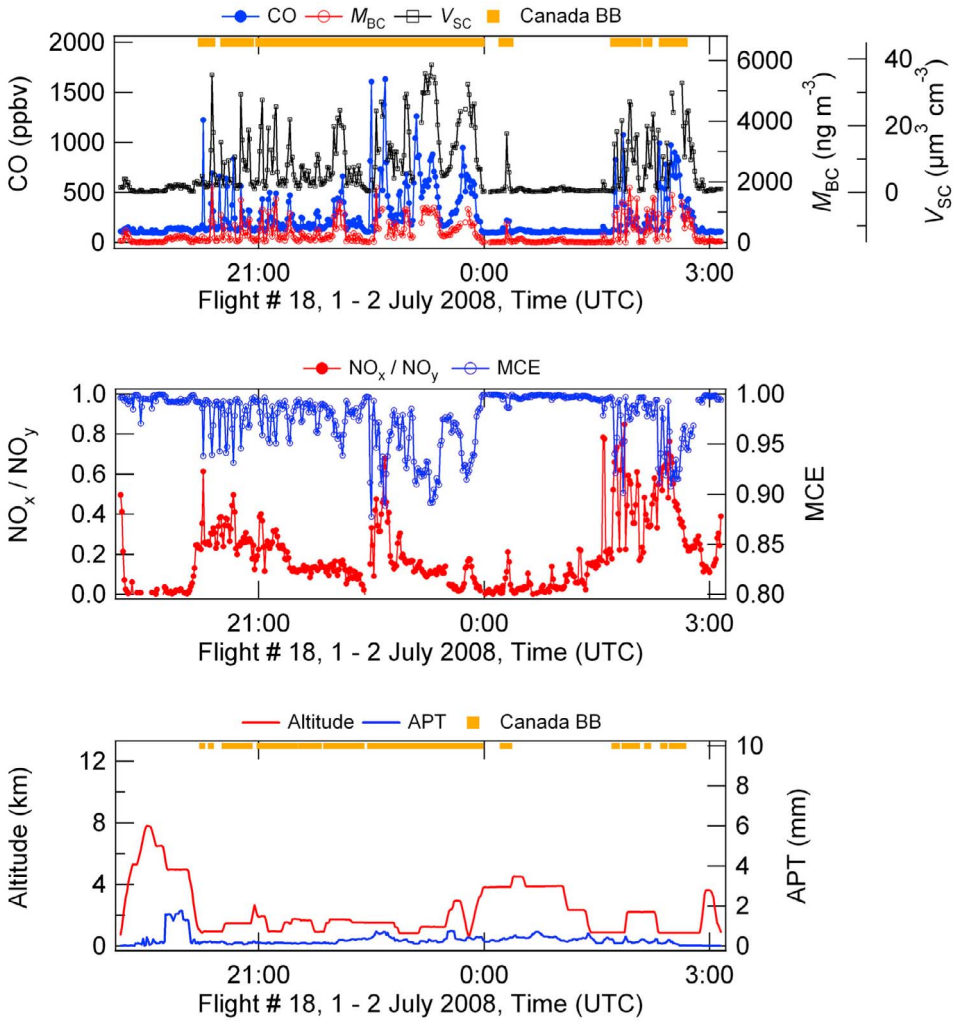

Figure 3. (top) Time series plots of CO, BC mass concentration (M_{BC}), volume concentration of LSP (V_{SC}), and identification of BB plumes. (middle) MCE and NO_x/NO_y ratio. (bottom) Precipitation (APT) and altitude of the DC-8 on 1–2 July.

average CMD and σ_{gc} are summarized in Table 3. The MMD of BC and volume median diameters (VMD) of LSP were 187 ± 10 nm and 294 ± 42 nm, respectively. Table 3 summarizes these values, together with the geometric standard deviations (σ_{gm} or σ_{gv}) of these size distributions. The average fractions of the unmeasured M_{BC} and V_{SC} values ($D_{BC} < 80$ nm and $D_{scat} < 185$ nm) were estimated to be 4% and 18%, respectively.

[34] We also derived the median shell/core ratios (D_p/D_{BC}) of BC for $D_{BC} > 200$ nm every 1 min. The median value of the D_p/D_{BC} was 1.48 (1.42 for smoldering phase and 1.62 for flaming phase (Table 3)). Possible causes of the dependence of D_p/D_{BC} on MCE are discussed in section 8. The estimated value using the above median of V_p/V_{BC} ($=D_p^3/D_{BC}^3$) is 3.24 (2.86 for smoldering phase and 4.25 for flaming phase). Thus BC represents about 0.31 (=1/3.24) of the volume (ranging from 0.23 to 0.35 for flaming and smoldering, respectively) of the particles that contain BC. We made more detailed analysis of the dependence of the microphysical parameters of BC on MCE in section 8.

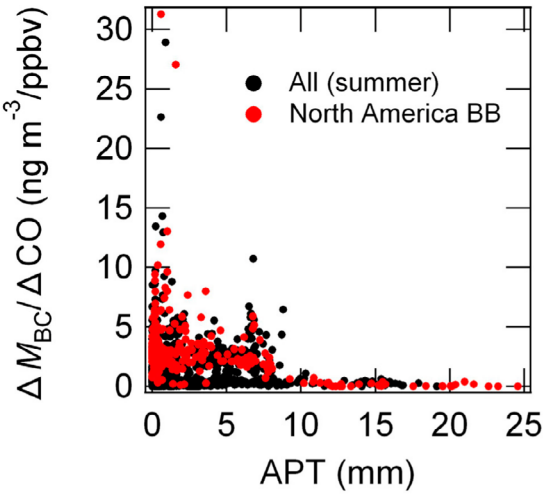

Figure 4. $M_{BC}/\Delta CO$ ratios plotted versus APT during ARCTAS-B. The APT was calculated for 24 h prior to aircraft sampling.

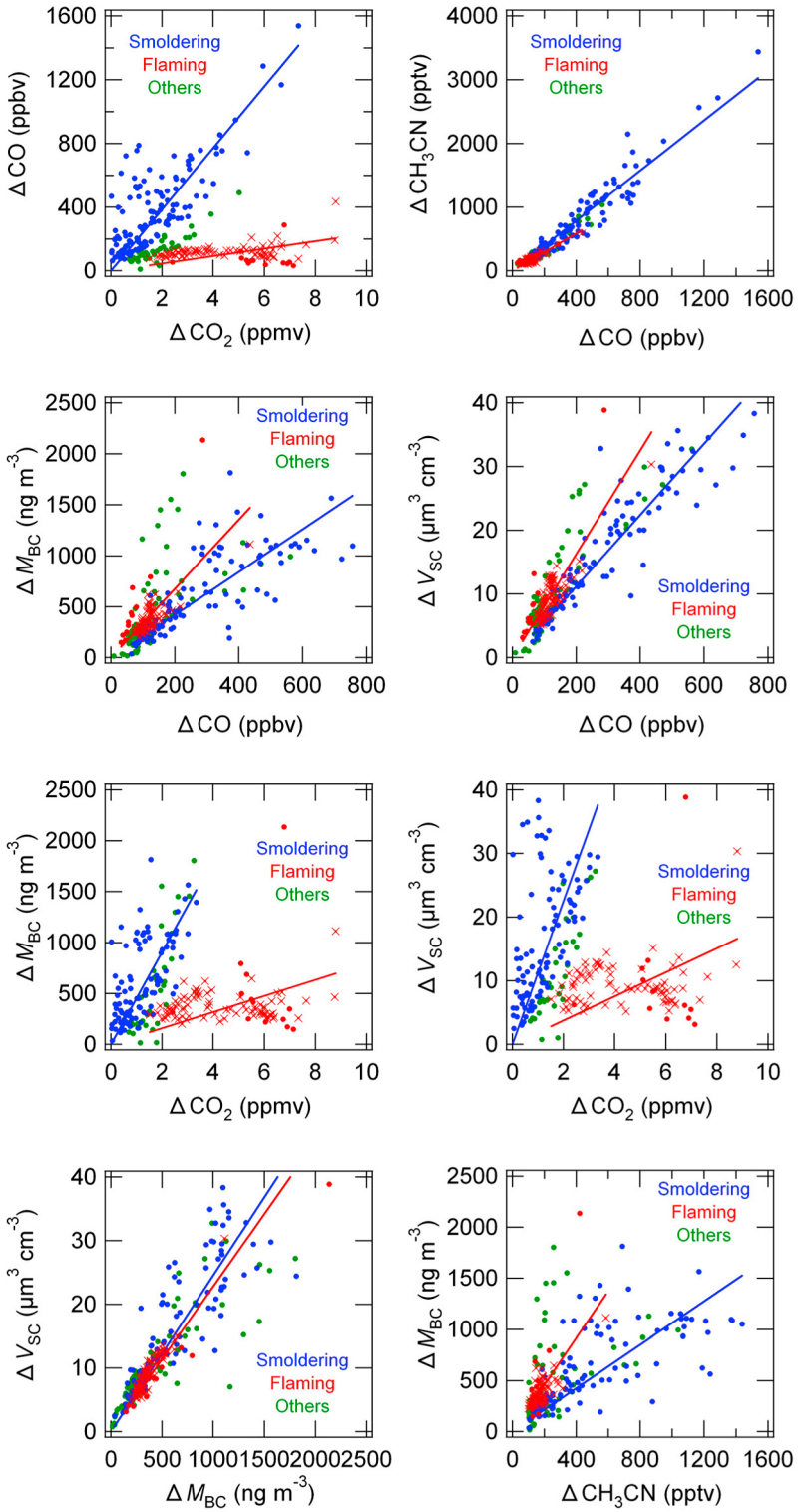

Figure 5. Correlations between M_{BC}, V_{SC}, ΔCO_2, ΔCO, and CH_3CN in wildfire plumes over Canada (circles) and California (crosses) during ARCTAS-B with APT < 1 mm. The data points are color coded for smoldering phase (MCE < 0.9; blue), flaming phase (MCE > 0.95: red), and others (0.90 < MCE < 0.95; green).

[35] Figure 8 and Tables 4 and 5 show the average mass concentrations and mass fractions of submicron non-refractory chemical components and BC in the extracted BB plumes as measured by the High-Resolution Time-of-Flight Aerosol Mass Spectrometer (HR-ToF-AMS) [*DeCarlo et al.*, 2006; *Dunlea et al.*, 2009] and SP2 on board the DC-8. The mass concentrations are in the units of μg STP m^{-3}. The average V_{SC}/M_{BC} and V_{SC}/V_{BC} ratios in the North American

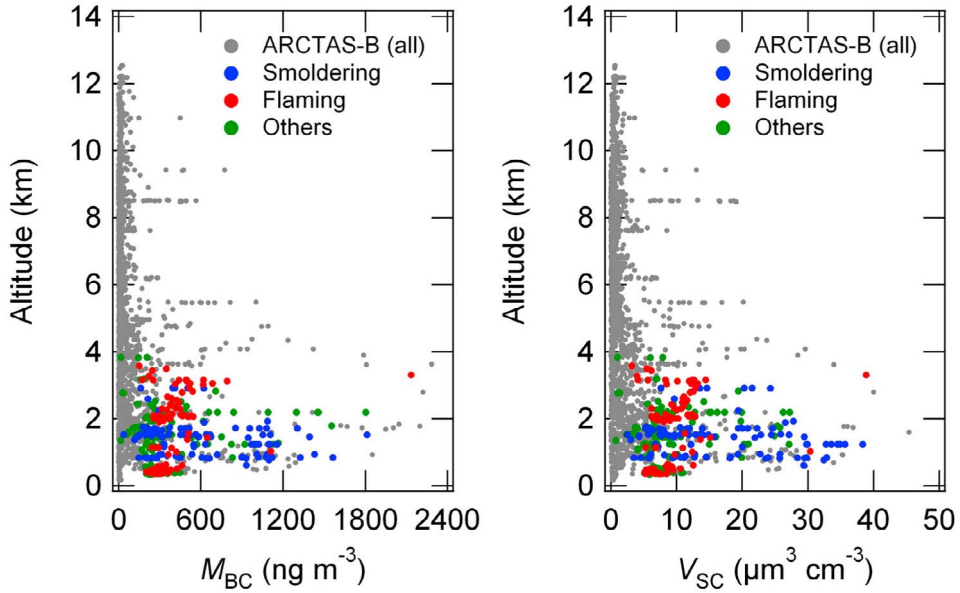

Figure 6. Vertical profiles of (left) M_{BC} and (right) V_{SC} for all data points measured over Canada during the ARCTAS-B campaign. The mass concentration of aerosols with density of 1 g cm^{-3} is 1 μg m^{-3} for a volume concentration of 1 μm^3 cm^{-3}.

plumes are summarized in Table 6. The uncertainties are given as the errors in the determinations of the slopes of the correlations shown in Figures 5 and 11. The prescribed measurement errors are not included in this uncertainty estimate.

[36] On average, OA constituted about 83% of the total mass concentration of BC and nonrefractory aerosol with a D_{va} (vacuum aerodynamic diameter [see *DeCarlo et al.*, 2004]) smaller than about 1 μm (PM_1). We therefore infer that V_{SC} in the plumes approximately represents the volume concentration of OA. M_{BC} was converted to BC volume concentration (V_{BC}) assuming ρ_{BC} = 2 g cm^{-3}. The average V_{SC}/M_{BC} and V_{SC}/V_{BC} ratios in the PM_1 range are summarized in Table 6. The average volume fraction of BC was about 0.02. Together with the result above that the volume fraction of BC was 0.31 for particles containing BC, this indicates that the large majority of the scattering particles measured by SP2 in the size range of 200 nm < D_p < 750 nm did not contain BC with D_{BC} > 80 nm, which is consistent with the particle number observations with the SP2.

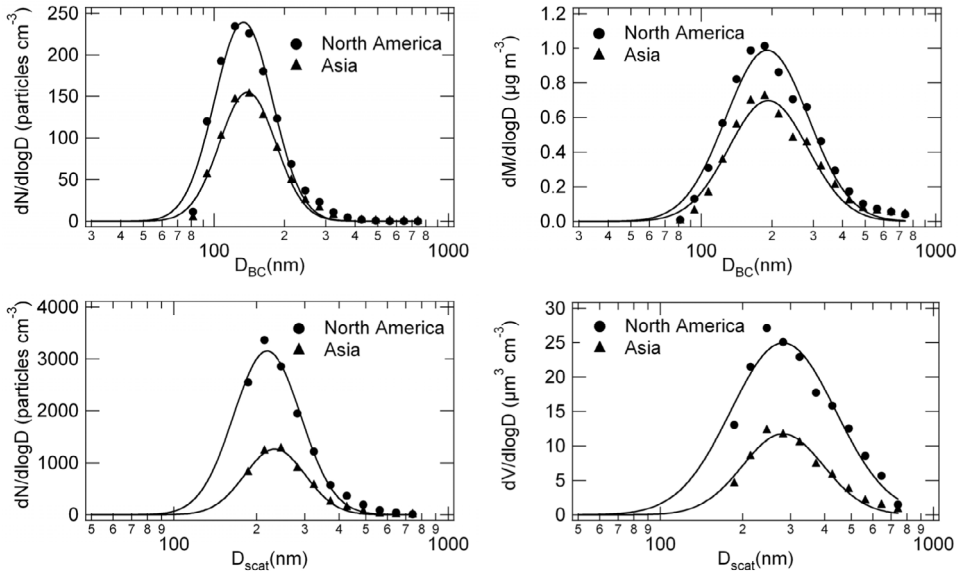

Figure 7. Mean distributions for (top) BC in number and mass space and (bottom) LSP in number and volume space, averaged for eight major forest fire plumes encountered in Canada during ARCTAS-B and those in BB fire plumes transported from Asia. Solid fitted lines are lognormal distribution functions.

Table 3. Size Distributions of BC and LSP

	Asia	Canada
	BC	
CMD	141 ± 8 nm	136 ± 6 nm
σ_{gc}	1.37 ± 0.04	1.32 ± 0.01
MMD	207 ± 31 nm	187 ± 10 nm
σ_{gm}	1.54 ± 0.1	1.48 ± 0.04
D_p/D_{BC}	1.52	1.48
	LSP	
CMD	238 ± 11 nm	224 ± 14 nm
σ_{gc}	1.31 ± 0.03	1.33 ± 0.05
VMD	306 ± 40 nm	294 ± 42 nm
σ_{gv}	1.46 ± 0.1	1.58 ± 0.08

[37] Figure 5 shows the correlations between ΔCO_2, ΔCO, ΔCH_3CN, ΔM_{BC}, and ΔV_{SC}. The correlations (ΔCO-ΔCO_2, ΔCH_3CN-ΔCO, ΔM_{BC}-ΔCO_2, ΔV_{SC}-ΔCO_2, ΔM_{BC}-ΔCO, ΔV_{SC}-ΔCO, and ΔV_{SC}-ΔM_{BC}) are color coded by the phase of BB. The least squares fits were made for each phase and were constrained through the origin. The flaming phase data obtained in Canada (red circles) and California (red crosses) showed no significant differences. The variability in the slopes was smallest for the ΔCH_3CN-ΔCO correlation. The correlation depended little on the phase of BB.

4. Aerosols in Plumes Transported From Asia (Siberia and Kazakhstan)

[38] Figure 9 shows time series plots of CO, M_{BC}, V_{SC}, and altitude of the DC-8, measured on 12–13 April (F#8). The M_{BC} and V_{SC} values were enhanced during the encounters with wildfire plumes. The time periods of sampling plumes of different origins in Asia are also shown in Figure 9. The plumes of the different origins appear as a number of interleaved spikes.

[39] We extracted data from air masses strongly influenced by biomass burning in Asia (Siberia and Kazakhstan). Most of the air masses enhanced in ΔM_{BC} and ΔV_{SC} were transported from Asia in 4.5 ± 2.1 days according to the calculated 10 day back trajectories.

[40] Figure 10 shows the $\Delta M_{BC}/\Delta CO$ correlation versus the estimated APT that the air masses experienced. Generally BB plumes transported from Asia in spring experienced small amounts of APT. The observed $\Delta M_{BC}/\Delta CO$ correlation tends to decrease with APT, especially for APT > 20 mm. We used the data with APT < 10 mm for the analysis of the emission ratios to minimize the possible effect of wet removal during transport. The slopes changed little by selecting data with APT < 5 mm, although the number of data points was greatly reduced.

[41] Figure 8 and Tables 4 and 5 show the average mass concentrations and mass fractions of PM_1 nonrefractory components of aerosol and BC in the Asian BB plumes measured by HR-ToF-AMS and SP2. OA constituted the dominant fraction (about 60%) of the nonrefractory components, similar to the Canadian BB plumes. However, the sulfate mass fraction was as large as about 30%, which is much larger than that for the North American plumes (3%–8%). It is very likely that SO_2 emitted from biomass burning was oxidized to form sulfate during transport. Formation of sulfate is discussed in more detail in section 7.

[42] Table 6 shows the average V_{SC}/M_{BC} and V_{SC}/V_{BC} ratios in the Asian plumes, restricted to low APT. These ratios were about 2 times lower than those in the Canadian plumes. The conclusion that most of the light-scattering particles did not contain BC is still valid. The difference in the BC fractions is discussed in terms of the differences in the conditions of combustion in section 6.

[43] The total mass concentrations of nonrefractory components measured by the AMS (M_{AMS}) were highly correlated with V_{SC}, with $r^2 = 0.89$ and 0.84 for ARCTAS-A and B, respectively. The average densities of nonrefractory components derived from the least squares fits of the M_{AMS}-V_{SC} were 1.33 and 1.54 g cm^{-3} for ARCTAS-A and B, respectively.

[44] Aerosols strongly influenced by BB have been shown to act as cloud condensation nuclei (CCN) [e.g., *Hallett et al.*, 1989; *Vestin et al.*, 2007; *Fors et al.*, 2010] due to the water solubility of some organic compounds. Therefore, the BC particles (thickly coated) in the Canadian and Asian plumes will act as CCN. It is likely that BC particles from Asia were also coated by sulfate, leading to higher CCN activity because of the high hygroscopicity of sulfate [e.g., *Petters and Kreidenweis*, 2007]. However, actual BC removal by precipitation depends on the timing of precipitation with respect to the formation of sulfate during transport. It is therefore difficult to compare the efficiency of wet removal BC particles in Canadian and Asian plumes.

[45] Figure 11 shows the correlations between ΔCO_2, ΔCO, CH_3CN, ΔM_{BC}, and ΔV_{SC} of the plumes (with

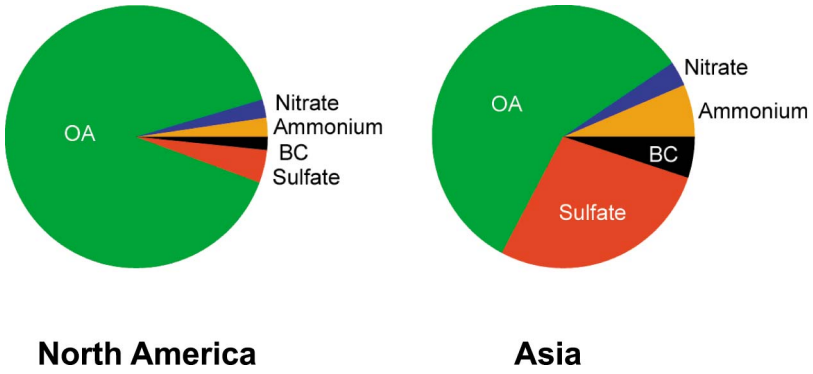

Figure 8. Fractions of major chemical components of aerosols measured by AMS in major forest fire plumes in (left) Canada and (right) Asia.

Table 4. Concentrations of Species for BB Plumes During ARCTAS and CARB

Species	Units	Asia BB, ARCTAS-A, All, Flaming	NA BB, ARCTAS-B			Canada BB, ARCTAS-B, MCE > 0.95, Flaming (4 July)	CA BB, CARB		
			All	MCE < 0.90, Smoldering (1 July)	MCE > 0.95, Flaming (4 and 13 July)		All	MCE < 0.90, Smoldering	MCE > 0.95, Flaming
Number		89	353	125	96	13	105	26	50
ΔCO	ppbv	40.8	124	328	111	54.7	125	413	90.6
ΔCO_2	ppmv	2.79	2.17	1.33	4.36	5.57	2.51	1.89	2.78
ΔCH_3CN	pptv	85.3	194	536	170	141	211	570	163
BC	ng m^{-3}	273	331	517	348	348	298	1240	280
LSP	μm^3 cm^{-3}	3.51	8.78	13.6	8.74	6.21	8.57	22.7	5.56
Shell/core ratio	–	1.52	1.48	1.42	1.62	1.63	1.51	1.56	1.46
Cl^-	μg m^{-3}	0.0192	0.0253	0.0653	0.0135	0.0258	0.0472	0.0848	0.0351
NH_4^+	μg m^{-3}	0.398	0.674	0.812	0.534	0.564	0.383	0.743	0.325
NO_3^-	μg m^{-3}	0.138	0.259	0.847	0.13	0.427	0.226	0.553	0.151
SO_4^{2-}	μg m^{-3}	1.67	1.2	1.19	0.921	0.951	0.607	1.09	0.49
SO_x	μg m^{-3}	2.02	1.78	1.75	2.42	1.06	1.85	4.49	1.52
Org	μg m^{-3}	3.69	12.2	40.5	9.11	8.7	9.55	46.5	8.46
PM_1 sum	μg m^{-3}	6.19	14.69	43.93	11.06	11.02	11.11	50.21	9.74
PM_1 + Av SO_2		6.54	15.27	44.49	12.56	11.13	12.36	53.61	10.77
NO	pptv	15.4	51.3	46.6	64.9	17.3	60.7	39.7	64.1
NO_2	pptv	16.5	153	171	221	41	287	371	236
NO_y	pptv	881	1158	1598	1582	845	1970	3067	1637
HNO_3	pptv	15.6	110	43.6	449	179	463	516	463
PAN	pptv	498	405	712	349	422	400	922	237
NO_x/NO_y	–	0.0362	0.176	0.136	0.181	0.069	0.176	0.134	0.183
SO_2(CIT)	pptv	91.9	144	131	532	NA	294	794	246
SO_2	pptv	73.6	126	129	170	24.6	292	794	235
Average SO_2	pptv	83	135	130	351	24.6	293	794	241
$SO_2/\Delta CO$	pptv/ppbv	2.0	1.1	0.39	3.2	0.45	2.3	1.9	2.7
$SO_x/\Delta CO$	pptv/ppbv	11	3.2	1.2	5	4.3	3.3	2.5	3.9
SO_2 as SO_4^{2-}	μg m^{-3}	0.35	0.58	0.56	1.5	0.11	1.25	3.4	1.03
DMS	pptv	NA	6	8	2.83	NA	7.5	20	6

APT < 10 mm) transported from Siberia and Kazakhstan during the ARCTAS-A period. We defined mixed air masses as those in which the trajectories passed over both regions. The plumes from the different source regions in Asia were classified and are color coded in Figure 11. The correlations of air masses transported from Kazakhstan and Siberia did not show significant differences. The results were the same even if we used the data set without discrimination by APT. Because of the small differences between Siberian and Kazakhstan air masses, we grouped these and mixed air masses as the Asian air masses for the statistical analysis discussed hereafter.

[46] *Warneke et al.* [2009] have shown significant differences in the slopes of correlations between various atmospheric species (e.g., CH_3CN-CO, ΔM_{BC}-ΔCO, ΔCO-ΔCO_2, OA (ΔV_{SC})-ΔCO) for plumes originating from Siberia and Kazakhstan by using the Lagrangian particle dispersion model FLEXPART [*Stohl et al.* 2005]. The reasons for the difference between theirs and the present results are not understood, although it may be partly due to the difference in identifying the source regions by using different methods or to variability within each source region coupled with the sampling of different plumes by the two aircraft.

[47] It should be noted that the $\Delta CO/\Delta CO_2$ ratios can change during the course of dilution of the BB plumes through mixing with ambient air [e.g., *Takegawa et al.*, 2003, 2004]. The effect of dilution can be larger for longer-lived species with higher background values, such as CO_2. Initial changes in the $\Delta CO/\Delta CO_2$ ratios of the BB plumes occur when they are injected into the FT. However, generally ΔCO_2 and ΔCO in the BB plumes are much larger than the difference in the background CO_2 and CO mixing

Table 5. Averages and Standard Deviations of the Ratios of Mass Concentrations of BC, Inorganic, and Organic Aerosols to PM1 in wt % for the Smoldering (MCE < 0.90) and Flaming Phases (MCE > 0.95) During ARCTAS and CARB

Species	Asia, All	ARCTAS-B			CARB		
		All	MCE < 0.90 (1 July)	MCE > 0.95 (4 and 13 July)	All	MCE < 0.90	MCE > 0.95
BC	4.9 ± 1.1	2.7 ± 2.9	1.7 ± 0.6	3.4 ± 0.6	2.5 ± 1.0	1.9 ± 0.2	2.8 ± 1.2
Cl^-	0.3 ± 0.2	0.2 ± 0.2	0.2 ± 0.1	0.1 ± 0.1	0.4 ± 0.2	0.6 ± 0.2	0.4 ± 0.1
NH_4^+	6.1 ± 1.7	3.6 ± 2.6	1.7 ± 0.6	4.8 ± 2.5	3.8 ± 1.5	5.5 ± 0.8	3.8 ± 1.5
NO_3^-	2.6 ± 1.6	1.8 ± 1.7	1.9 ± 0.7	1.7 ± 1.5	1.4 ± 1.0	1.2 ± 0.2	1.6 ± 1.0
SO_4^{2-}	29.6 ± 9.1	7.7 ± 7.1	2.8 ± 0.9	9.8 ± 7.1	8.0 ± 4.8	13.0 ± 2.3	8.0 ± 4.6
SO_4^{2-} + SO_2	31.1 ± 9.6	11.9 ± 1.3	4.0 ± 1.3	20.0 ± 14.8	15.6 ± 9.4	19.6 ± 3.5	14.8 ± 8.5
Org	56.3 ± 8.6	84.2 ± 11.4	91.7 ± 1.8	80.3 ± 9.6	83.9 ± 6.5	77.8 ± 3.0	83.5 ± 6.5

Table 6. Emission Ratios of BC, CO, CO_2, and CH_3CN for Biomass Burning[a]

Species	Asia BB, ARCTAS-A, All, Flaming	NA BB, ARCTAS-B			CA BB, CARB, All, Mix	Kazakhstan,[b] ARCPAC	Lake Baikal,[b] ARCPAC	*Andreae and Merlet* [2001], Mix	CA FF,[c] CARB	Tokyo FF,[d] 2009
		All, Mix	MCE < 0.90, Smoldering	MCE > 0.95, Flaming						
CO/CO_2 (ppbv/ppmv)	15 ± 5	80 ± 110	222 ± 118	26 ± 10	114 ± 23	50 ± 25	42 ± 19	107 ± 38	5.2 ± 0.9	11
M_{BC}/CO (ng m^{-3}/ppbv)	8.5 ± 5.4	2.3 ± 2.2	1.7 ± 0.8	3.4 ± 1.6	3.4 ± 1.4	10 ± 5	7 ± 4	6.5 ± 3.2	3.1 ± 1.0	5.7
M_{BC}/CO_2 (ng m^{-3}/ppmv)	129 ± 67	180 ± 269	369 ± 257	88 ± 80	236 ± 103	NA	NA	701 ± 245	16.2 ± 8.2	62
M_{BC}/CH_3CN (ng m^{-3}/pptv)	3.9 ± 2.1	1.2 ± 1.4	0.88 ± 0.6	2.2 ± 1.3	1.7 ± 0.6	NA	NA	NA	Nil	Nil
CH_3CN/CO (pptv/ppbv)	2.2 ± 1.6	1.8 ± 0.4	1.9 ± 0.4	1.6 ± 0.74	1.7 ± 0.4	NA	NA	NA	Nil	Nil
V_{SC}/M_{BC} (cm^3 m^{-3}/g m^{-3})	12 ± 3	24 ± 6	26 ± 7	24 ± 6	23 ± 6	NA	NA	NA	5 ± 3	NA
V_{SC}/V_{BC} (cm^3/cm^3)	24 ± 6	48 ± 12	52 ± 14	48 ± 12	46 ± 12	NA	NA	NA	10 ± 6	NA
V_{SC}/CO (μm^3 cm^{-3}/ppbv)	10 ± 2.3	5.4 ± 1.6	4.4 ± 2.3	8.3 ± 4.3	–	NA	NA	NA	NA	NA
V_{SC}/CO_2 (μm^3 cm^{-3}/ppmv)	1.6 ± 0.7	4.4 ± 4.0	9.6 ± 8.0	2.1 ± 0.9	–	NA	NA	NA	NA	NA

[a]The mass concentrations are in units of μg STP m^{-3}.
[b]*Warneke et al.* [2009].
[c]Fossil fuel combustion in California.
[d]Fossil fuel combustion in Tokyo [*Kondo et al.*, 2010].

ratios between the BL and FT. Therefore, the changes in the slopes of the CO-CO_2 correlations by this process should be small.

[48] Larger changes in the $\Delta CO/\Delta CO_2$ ratios are considered to occur by mixing of the diluted BB plumes with ambient air during the long-range transport in the FT. The average CO_2 mixing ratios at the surface and in the FT were observed to increase by about 1 ppmv between 50°N and 70°N [e.g., *Komhyr et al.*, 1985; *Tans et al.*, 1989; *Anderson et al.*, 1996]. In addition, the mean CO_2 mixing ratios of the 1 km averaged values between 2 and 7 km were 391.7 ± 0.7 ppmv during ARCTAS-A. If 50% of the BB plumes are mixed with ambient air during transport from 50°N to 70°N, the CO_2 mixing ratio of the mixed air is anticipated to increase by 0.5 ppmv on average. This leads to an uncertainty of the $\Delta CO/\Delta CO_2$ ratios of about 15%–20% for the average ΔCO_2 of 2.8 ppmv (Table 4), giving a measure of the uncertainties in the derived $\Delta CO/\Delta CO_2$ for the Asian BB plumes.

[49] The size distributions of BC and LSP in the plumes from Asia (APT < 10 mm) are shown in Figure 7. The CMD and MMD (VMD) of the lognormal fitted BC and LSP size distributions together with the values of the standard deviations are summarized in Table 3. The values for the plumes from Siberia and Kazakhstan were very similar. Therefore they were grouped together and labeled as Asian. The variability of these parameters was small. The median D_p/D_{BC} ratios for the Asian plumes was 1.52 (corresponding

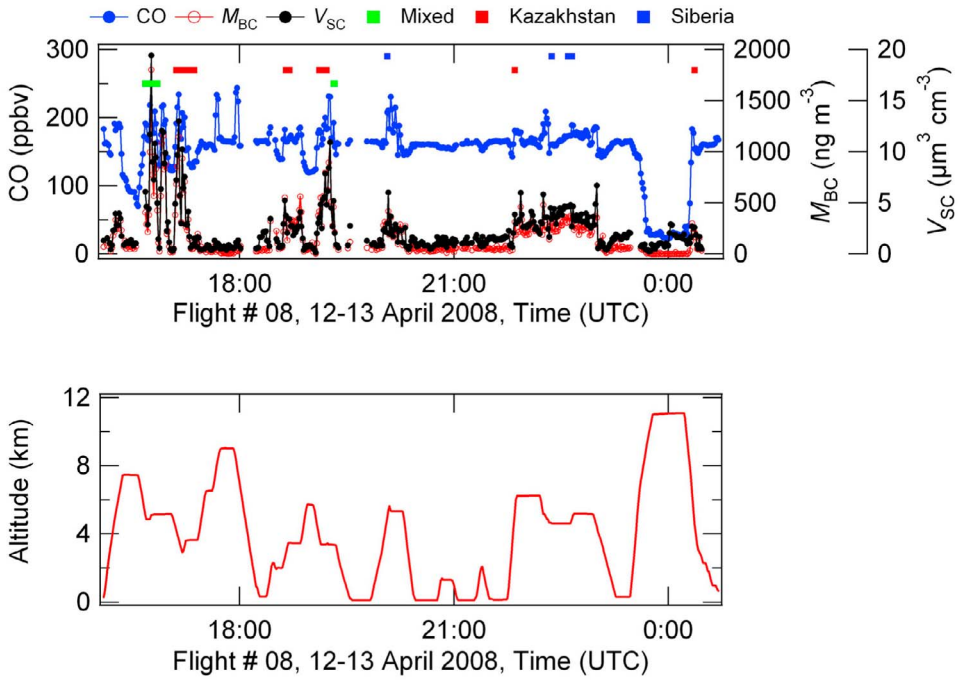

Figure 9. Time series plots of CO, BC mass concentration (M_{BC}), and volume concentration of LSP (V_{SC}) measured over Alaska on 12–13 April. Bars indicate the periods when the plumes from the respective region were sampled.

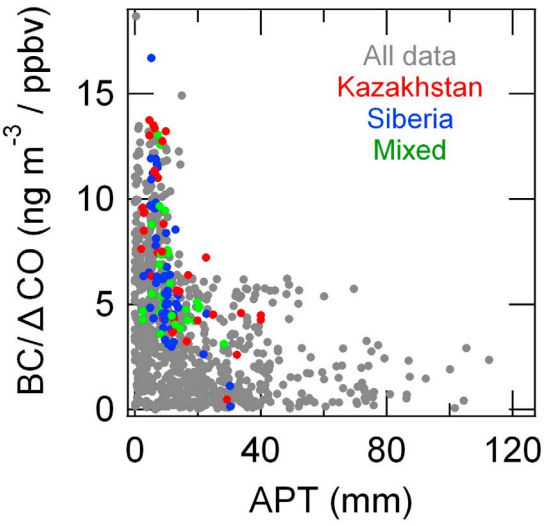

Figure 10. $M_{BC}/\Delta CO$ ratios plotted versus APT during ARCTAS-A.

to a BC volume fraction of 0.28 for BC-containing particles), indicating that the BC particles were thickly coated. The size distributions of BC and LSP and the D_p/D_{BC} ratios of the Asian fire plumes were very similar to those of the North American fire plumes (Figure 7), despite the significant differences in the emission ratios, including the $\Delta CO/\Delta CO_2$ ratios.

5. Average Emission Ratios

[50] We derived the emission ratios between M_{BC}, V_{SC}, CH_3CN, CO, and CO_2 averaged over the measurement period during ARCTAS-B. The averaging method described by *Andreae and Merlet* [2001] was used for this purpose. Namely, the net increases of species X and Y above their background values in the jth plume were first calculated (ΔX_j and ΔY_j). Then the sums for all the plumes were calculated, i.e., $\Delta X = \sum_j \Delta X_j$ and $\Delta Y = \sum_j \Delta Y_j$. The average emission ratio of X versus Y was given as $ER_{av} = \Delta X/\Delta Y$. We note that for V_{SC} the value derived is not strictly an "emission" ratio, as secondary inorganic (e.g., sulfate, as discussed above) and organic aerosol species [e.g., *DeCarlo et al.*, 2010] are formed during transport and solar exposure.

[51] We derived the emission ratios of CO/CO_2, M_{BC}/CO, M_{BC}/CO_2, M_{BC}/CH_3CN, CH_3CN/CO, V_{SC}/CO_2, V_{SC}/CO, and V_{SC}/M_{BC}, and they are summarized in Table 6. The large variability in M_{BC}/CO, M_{BC}/CO_2, and M_{BC}/CH_3CN are readily seen. The lower variabilities in the CH_3CN/CO emission ratio is also seen.

[52] The emission ratios for BB in Asia, discussed in section 4, were derived in the same way and are given in Table 6. In Table 6, we added the reported values for biomass burning in Asia for April 2008 during the ARCPAC Mission [*Warneke et al.*, 2009]. In addition, we also included the data for forest fires in California during ARCTAS-CARB in Table 6 for comparison.

[53] The average CO/CO_2 (or MCE) and M_{BC}/CO emission ratios were similar for wildfires during ARCTAS-B (Canada and California) with $\Delta CO/\Delta CO_2 = 80 \pm 100$ ppbv/ppmv and ARCTAS-CARB (California) with $\Delta CO/\Delta CO_2 = 114 \pm 23$ ppbv/ppmv. In the Asian plumes, the average CO/CO_2 emission ratios were much smaller with $\Delta CO/\Delta CO_2 = 15 \pm 5$ ppbv/ppmv, and the M_{BC}/CO emission ratios were a few times larger, although the M_{BC}/CO_2 emission ratios were similar.

[54] Estimates of the emission ratios for biomass burning in previous studies were compiled by *Andreae and Merlet* [2001]. The compiled values for temperate forests are also listed in Table 6. The present M_{BC}/CO and M_{BC}/CO_2 emission ratios for wild fires in North America are lower than the compiled value by a factor of 2–4, although the CO/CO_2 emission ratio was close to their estimates. The derived M_{BC}/CO emission ratio for BB plumes from Asia was much closer to the compiled value, although the observed M_{BC}/CO_2 emission ratio was about 5 times lower.

[55] Table 6 also shows the V_{SC}/M_{BC} ratios observed in plumes strongly influenced by emissions by combustion of fossil fuel in California (ARCTAS-CARB) and in Tokyo in August–September 2009 [*Kondo et al.*, 2011]. These data were taken from the same SP2 calibrated in the same way, enabling direct comparison. The comparison shows that much larger volumes of LSP relative to those of BC were coemitted with BC from the wildfires than those from fossil fuel combustion. Generally the emission ratios of primary organic aerosols to BC have been reported to be of the order of 1 when scaled with the mass concentrations [*Takegawa et al.*, 2006] for fossil fuel combustion, consistent with the V_{SC}/V_{BC} ratio for Tokyo in Table 6. The variability in the V_{SC}/M_{BC} ratios in Tokyo was caused mainly by the formation of secondary aerosols (organic and inorganic) [e.g., *Kondo et al.*, 2011], consistent with results at many other locations [*de Gouw and Jimenez*, 2009].

[56] OA/BC ratios were observed for aerosol particles emitted from crown fires in Canadian wildfires in a previous study [*Conny and Slater*, 2002]. These authors report that BC/TC (OC + BC) ratios were 0.085 and 0.0087 for the flaming and smoldering stages, respectively. The corresponding OC/BC ratios were about 10 and 100 for these stages, consistent with the present results. OA/BC and OC/BC mass ratios of about 6 and 4 were observed in agricultural fire plumes in the Yucatan [*Yokelson et al.*, 2009]. These ratios are much lower than the present results and those reported by *Conny and Slater* [2002].

6. Dependence of the Emission Ratios on MCE

6.1. Injection Height

[57] The injection heights of the plumes formed in different phases of burning can vary because of the difference in the thermal energy release as a function of the burning phase. This point was suggested by *Andreae and Merlet* [2001] but has not been fully demonstrated by observed atmospheric species. To investigate this possible effect, the sampling altitudes of the plumes are plotted versus the $\Delta CO/\Delta CO_2$ ratios and MCE in Figure 12. It is seen that the $\Delta CO/\Delta CO_2$ ratios decreased and MCE increased with altitude, indicating a strong dependence of these parameters on the phase of burning.

[58] The thermal energy received by the plumes during burning increases their potential temperature (PT) from an average surface value of θ_0 to θ_{fire}. The plumes with θ_{fire} ($>\theta_0$)

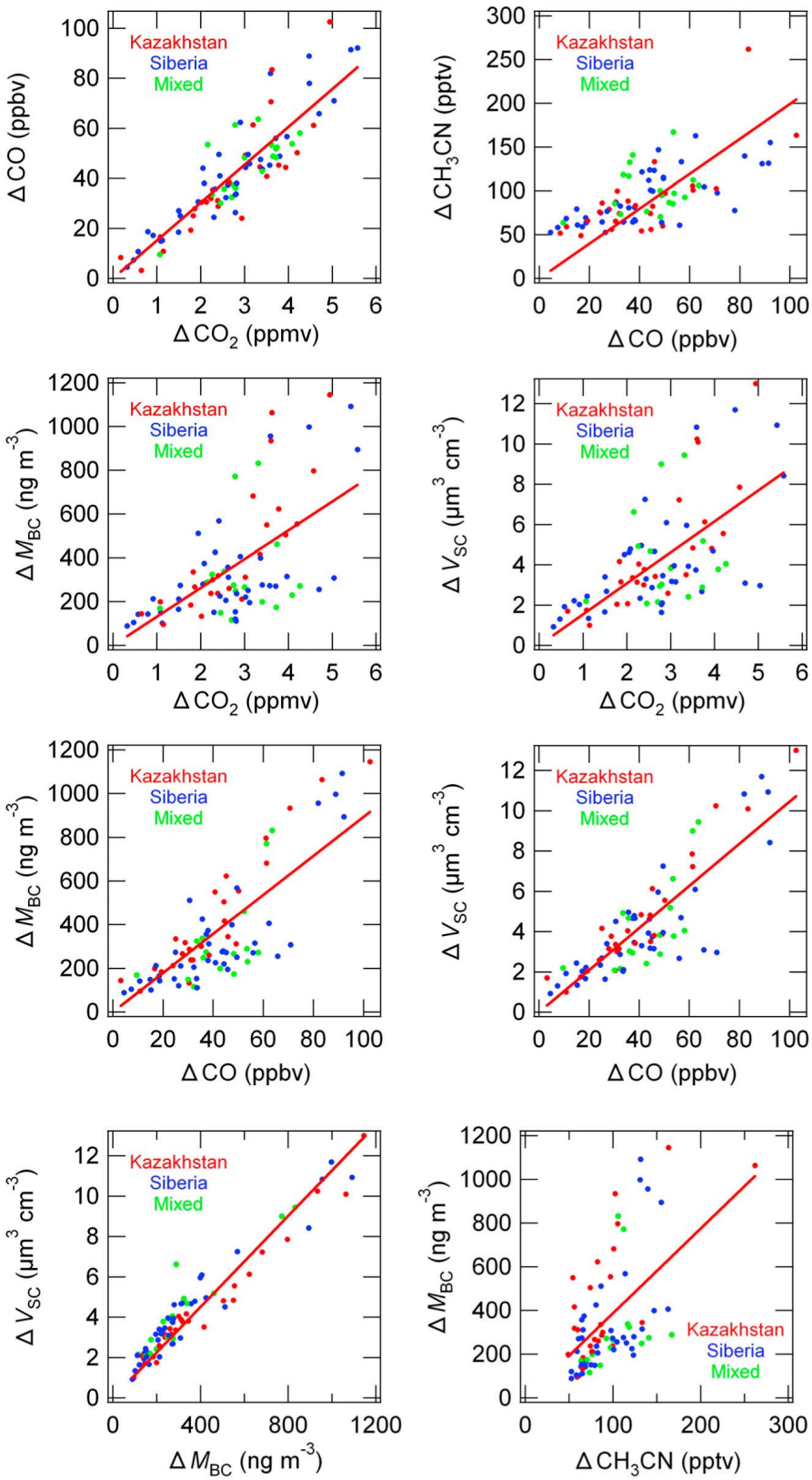

Figure 11. Correlations between M_{BC}, V_{SC}, ΔCO_2, ΔCO, and CH_3CN observed in major wildfire plumes that experienced little precipitation during transport from Asia to Alaska (ARCTAS-A). The least squares linear regression fits are shown by solid lines.

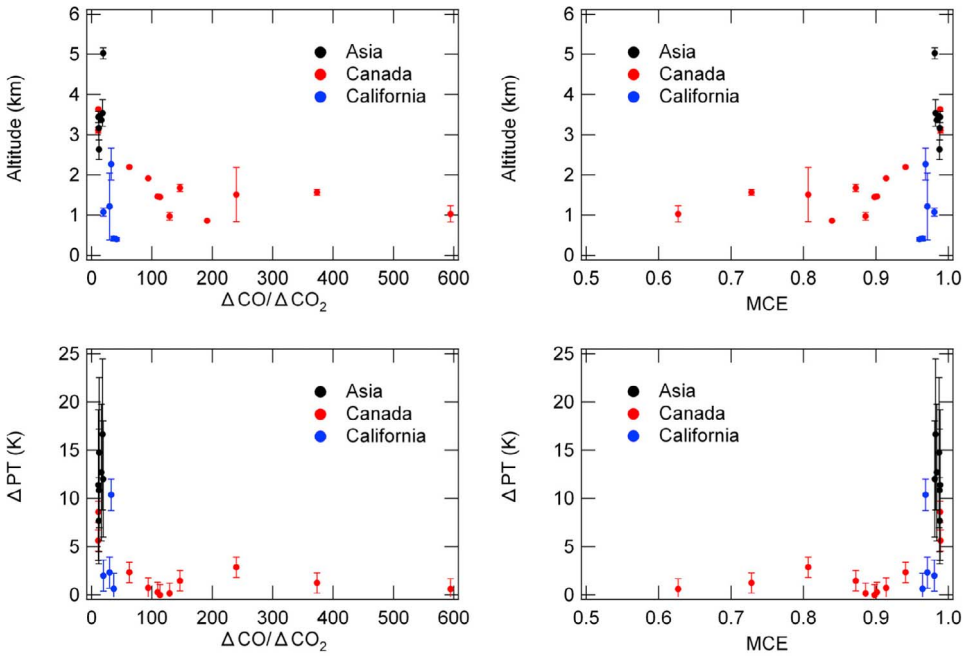

Figure 12. (top) Relationship between the sampling altitudes of the plumes versus $\Delta CO/\Delta CO_2$ ratios and MCE. Vertical bars represent the variability of the estimate. The least squares linear regression fits are also shown. (bottom) Relationships between the change in potential temperature (with reference to the surface level potential temperature) versus $\Delta CO/\Delta CO_2$ ratio and MCE.

gain buoyancy and ascend to the altitude where the *PT* of the ambient air (θ_a) is equal to θ_{fire}. Cloud formation will not substantially alter θ_{fire}, if clouds evaporate without precipitation. Therefore $\Delta\theta = \theta_a - \theta_0$ is considered to be proportional to the thermal energy gained per unit mass of the plume near the surface. We estimated $\Delta\theta$ by assuming that θ_a is the *PT* of the sampled plume and θ_0 is the average *PT* near the surface during each flight, for plumes sampled near the point of emission. Active mixing in the BL during daytime by solar heating of the surface will smooth out the vertical structure of $\Delta\theta$ produced by the thermal energy of combustion. Therefore the derived $\Delta\theta$ should be interpreted as a representation of the injection height that accounts for the vertical thermodynamic structure near the BB sources in North America.

[59] Figure 12 (bottom) shows the relationships of the $\Delta CO/\Delta CO_2$ ratio and MCE with $\Delta\theta$ for the North American plumes. The sharp increase in $\Delta\theta$ at MCE > 0.98 is clearly seen. Namely, a substantial increase in $\Delta\theta$ was detected only at the highest combustion efficiencies.

[60] For comparison, the data for the Asian plumes are also plotted in Figure 12. We estimated θ_0 for these plumes by combining the calculated trajectories and the surface *PT* of the burning areas in Asia estimated using NCEP data. The uncertainty of θ_0 was estimated from the variability in the temperature of the source region. Because we cannot narrow down the source region from the trajectory analysis, the uncertainty in θ_0 was as large as about 10 K. However, because the sampled plumes were injected directly into the FT, the uncertainty in estimating $\Delta\theta$ caused by mixing in the BL should be smaller than for the North American plumes measured in the BL. Despite this uncertainty, the increase in $\Delta\theta$ corresponded with an MCE as high as 0.98, similarly to the North American plumes.

[61] It is likely that plumes formed during the flaming phase were selectively injected to higher altitudes than those during the smoldering phase over Asia. The higher-altitude plumes were transported in shorter time to the sampling regions near Alaska, associated with higher wind speeds [*Fuelberg et al.*, 2010]. In other words, the $\Delta CO/\Delta CO_2$ ratios of the Asian plumes measured during ARCTAS-A may not represent the vertically averaged emission values in Asia. The estimation of relative contributions of the flaming and smoldering phases in producing aerosols and trace gases including CO will require data in the BL over Asia.

6.2. Emission Ratios

[62] We have attempted to interpret the large variability of the slopes of the ΔM_{BC}-ΔCO, ΔM_{BC}-ΔCO_2, ΔM_{BC}-ΔCH_3CN, ΔV_{SC}-ΔCO_2, ΔV_{SC}-ΔCO, and ΔV_{SC}-ΔM_{BC} correlations in terms of MCE. These ratios are plotted versus MCE in Figure 13. Standard deviations (1σ) of the 1 min data used to derive individual data points were calculated first. Table 7 summarizes the averages of the 1σ values and the average ratios for BB plumes in Asia, Canada, and California shown in Figure 13. The least squares fits were derived using the data sets with APT < 1 mm for Canada and California and APT < 5 mm for Asia. It should be noted that some of the emission ratios ($\Delta V_{SC}/\Delta CO_2$, $\Delta M_{BC}/\Delta CO_2$, $\Delta M_{BC}/\Delta CO$, $\Delta V_{SC}/\Delta CO$) are not independent of MCE, because the estimate of MCE contains ΔCO_2 and ΔCO.

[63] The $\Delta M_{BC}/\Delta CO$ ratio increased with the increase in MCE. This relation is important because the ratio is often used in estimating BC emissions and BC removal during

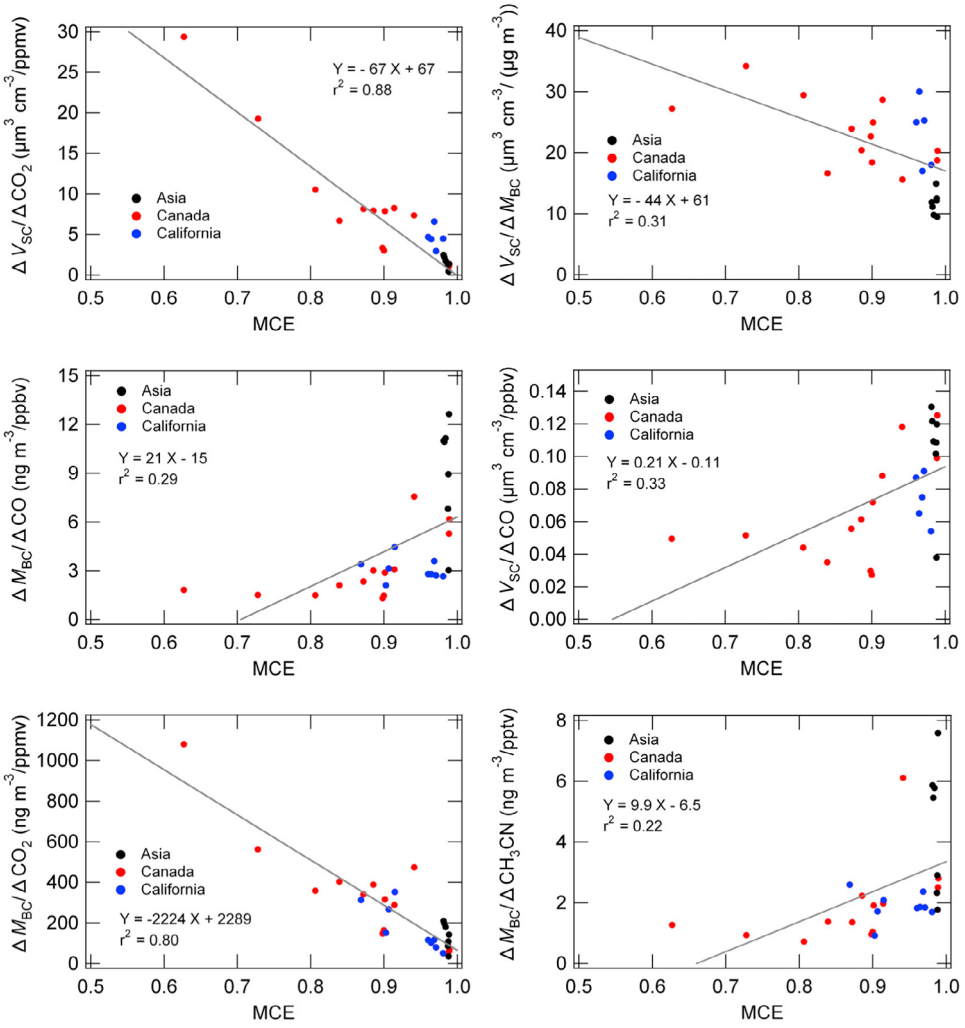

Figure 13. Scatterplots of M_{BC}/CO, M_{BC}/CO_2, M_{BC}/CH_3CN, CH_3CN/CO, V_{SC}/CO_2, V_{SC}/CO, and V_{SC}/M_{BC} ratios versus MCE. Linear regression fits using all the data points are also shown.

transport using CO as a tracer. Because of the large variability in the $\Delta M_{BC}/\Delta CO$ ratios, the estimates of BC removal based on downwind measurements of $\Delta M_{BC}/\Delta CO$ will have large uncertainty unless $\Delta M_{BC}/\Delta CO$ was measured at the source. In contrast, the $\Delta M_{BC}/\Delta CO_2$ and the $\Delta V_{SC}/\Delta CO_2$ ratios decreased with the increase in MCE. The $\Delta V_{SC}/\Delta M_{BC}$ ratios also decreased with the increase in MCE.

[64] For flaming fires, the lower $\Delta V_{SC}/\Delta M_{BC}$ ratios tend to lower the single scattering albedo (SSA) of the ensemble of aerosols. The thicker coating of BC for the flaming phase leads to amplified absorption as compared with that for externally mixed BC. The SSA of individual BC particles increases with the increase in the shell/core ratios because of the increase in the scattering cross section [*Oshima et al.*, 2009]. However, the amplified BC absorption leads to a decrease in the SSA of the ensemble of aerosols [e.g., *Shiraiwa et al.*, 2008; *Seinfeld and Pandis*, 2006, Figure 21.11]. For this reason, we expect a lower (higher) SSA in plumes of the flaming (smoldering) phase. In fact, the SSA at a wavelength of 538 nm was observed to decrease substantially with the increase in MCE in BB plumes in Brazil [*Reid and Hobbs*, 1998].

[65] The $\Delta M_{BC}/V_{SC}$ ($\Delta V_{SC}/\Delta M_{BC}$) ratio showed an almost exponential increase at MCE > 0.95. The rapid increase in BC/OC at MCE > 0.95 was observed by combustion facility experiments [*Christian et al.*, 2003], consistent with the present results, considering that OA is the dominant component of ΔV_{SC}.

[66] The $\Delta V_{SC}/\Delta CO$ ratios increased with the increase in MCE, although the correlation was not tight. The interpre-

Table 7. Averages of the 1σ Values (±) and the Average Ratios, MCE, and Shell/Core Ratios for BB Plumes in Asia, Canada, and California

	Asia	Canada	California
$\Delta V_{SC}/\Delta CO_2$	1.88 ± 0.40	7.97 ± 2.30	2.50 ± 1.16
$\Delta V_{SC}/\Delta M_{BC}$	0.0116 ± 0.0011	0.0261 ± 0.0053	0.0246 ± 0.0019
$\Delta M_{BC}/\Delta CO$	11.8 ± 4.5	3.25 ± 0.678	2.86 ± 0.35
$\Delta V_{SC}/\Delta CO$	0.133 ± 0.051	0.0749 ± 0.0116	0.0699 ± 0.0053
$\Delta M_{BC}/\Delta CO_2$	167 ± 37	357 ± 117	100 ± 48
$\Delta M_{BC}/\Delta CH_3CN$	5.16 ± 1.44	2.10 ± 0.56	2.12 ± 0.34
MCE	0.985 ± 0.0023	0.846 ± 0.060	0.961 ± 0.021
Shell/core ratio	1.54 ± 0.033	1.45 ± 0.026	1.51 ± 0.033

Table 8. Comparison of SO_2 and Sulfate Concentrations in Background Air and BB Plumes From Asia During ARCTAS-A With and Without Selection by APT

	Instrument	All	APT < 10 mm
	SO_2 (pptv)		
Background	CIT	98	116
	GIT	78	101
Asian BB	CIT	108	140
	GIT	81	105
	Sulfate ($\mu g\ m^{-3}$)		
Background	AMS	0.13	0.14
Asian BB	AMS	0.46	0.49

tation of this relationship is not straightforward because ΔV_{SC} and ΔCO are both smoldering products. This trend may be sensitive to the relative emissions (and secondary formation) of LSP and CO to those of CO_2 because both the $\Delta V_{SC}/\Delta CO_2$ and $\Delta CO/\Delta CO_2$ ratios decreased with the increase in MCE.

[67] A number of studies have shown the particle emission factor (g/kg) to decrease with the increase in MCE by burning tropical forest fuels in a combustion facility [*Ferek et al.*, 1998; *Yokelson et al.*, 2007, 2008]. The particle mass and fuel mass are approximately proportional to ΔV_{SC} and $\Delta CO_2 + \Delta CO$. Their results are qualitatively consistent with the present observations, although the types of fuels were different, namely tropical versus boreal forests. The agreement in the trend between our study and those of *Yokelson et al.* [2007, 2008] provides additional support for the methodology in using MCE in the interpretation of field data. The present analysis demonstrates the necessity of taking into account the dependence of the emission ratios of aerosols on the burning phase (e.g., MCE) in improving the uncertainty in estimating aerosol emissions from BB.

7. Formation of Sulfate

[68] Here we discuss sources of sulfate in BB plumes. First, it should be noted that air masses strongly impacted by anthropogenic activities were excluded using CH_2Cl_2 as a tracer throughout the present analysis, as discussed in section 2.4. This already minimizes the effects of SO_2 emissions from anthropogenic activity near the BB regions on the Canadian and Asian plumes.

[69] Second, we investigated the effect of mixing of BB air masses with air masses with unidentified origins, namely air masses that did not originate from identified regions of BB or anthropogenic emissions in the BL within 10 days. Table 8 summarizes the average SO_2 and sulfate concentrations in the background air and in the Asian BB plumes. The sulfate concentrations in the background air were 3–4 times lower than those in the Asian BB plumes, although the SO_2 concentrations were similar. Considering this, it is also unlikely that mixing of FT air caused elevated sulfate in the BB-impacted air masses during the transport from Asia in the FT.

[70] Now we discuss sources of sulfate in BB plumes based on the statistical data shown in Tables 4 and 5. In Tables 4 and 5, mass concentrations of sulfate, which can form from SO_2, are also shown. In the Canadian plumes, sulfate was only 3% of PM_1 in the smoldering phase, and it was higher (8%) in the flaming phase. However, the mass fraction of the observed PM_1 accounted for by sulfate plus potential sulfate = $(SO_4^{2-} + f \times SO_2)/(PM_1 + f \times SO_2)$ was as high as 20% for MCE > 95% and it remained low for MCE < 90%. Here $f = 4.28\ \mu g\ m^{-3}$/ppbv is the conversion factor from gas phase SO_2 concentrations in ppbv to equivalent sulfate mass concentrations in $\mu g\ m^{-3}$. The dependence of the $SO_x = SO_2 + SO_4^{2-}$ on MCE was similar for the CARB data. In the Asian plumes (flaming phase), SO_4^{2-} and SO_x constituted about 27% and 31% of PM_1, respectively.

[71] The comparison of BB in different regions also indicates that SO_x was emitted from BB most intensively in the flaming phase, as observed by *Ferek et al.* [1998]. A large fraction of the emitted SO_2 was oxidized to sulfate during transport from Asia to the Alaskan region (versus a much smaller oxidized fraction for the Canadian plumes), leading to the higher fraction of sulfate in the Asian plumes than those from the other regions. The longer time scale of oxidation of sulfate versus secondary organic aerosol (SOA) precursors also results in changing OA/sulfate ratios for anthropogenic pollution plumes, which first increase as SOA forms and then decrease as sulfate forms on a longer time scale [*Brock et al.*, 2008; *Dunlea et al.*, 2009].

[72] Emissions of SO_2 from BB were also observed in the Yucatan [*Yokelson et al.*, 2009] and in laboratory experiments simulating wildfires [*Yokelson et al.*, 1996; *Burling et al.*, 2010], while direct emission of sulfate has also been observed in similar laboratory experiments [*Lewis et al.*, 2009]. The fires in the Yucatan were primarily crop residue fires, similar to those in Kazakhstan. The emission ratios from these studies are somewhat higher than those estimated by *Andreae and Merlet* [2001]. The molar SO_2/CO emission ratios were about 2% in the Yucatan, and they were about 1%–2% for evergreen coniferous fuels [*Yokelson et al.*, 1996]. These SO_2/CO emission ratios are about an order of magnitude higher than the present observations. It is possible that the variations in SO_2 emissions between regions vary with the amount of sulfate and SO_2 deposited onto vegetation from the atmosphere and directly by farming, which will be larger for areas with large SO_2 sources (such as Mexico) and lower for areas without such large sources (such as Saskatchewan).

[73] DMS was also emitted by BB, as summarized in Table 4, although at levels 1–2 orders of magnitude lower than for SO_2. The DMS/SO_x ratios for Canadian plumes indicate more efficient DMS emissions in the smoldering phase than in the flaming phase. For the CARB data, the ratios were similar for smoldering and flaming phases. The increased emission of the reduced form of sulfur-containing species in the smoldering phase is in contrast to the increased emission of the oxidized form of sulfur (SO_2) from the flaming phase.

8. Microphysical Properties of BC and LSP

8.1. Size Distribution

[74] The number and mass (volume) size distributions of aerosols in the BB plumes from North America and Asia were fitted to a good approximation with lognormal size distribution functions, with typical examples shown in Figure 7. To a first approximation, these parameters were very similar in all the BB plumes. For more detailed investigations,

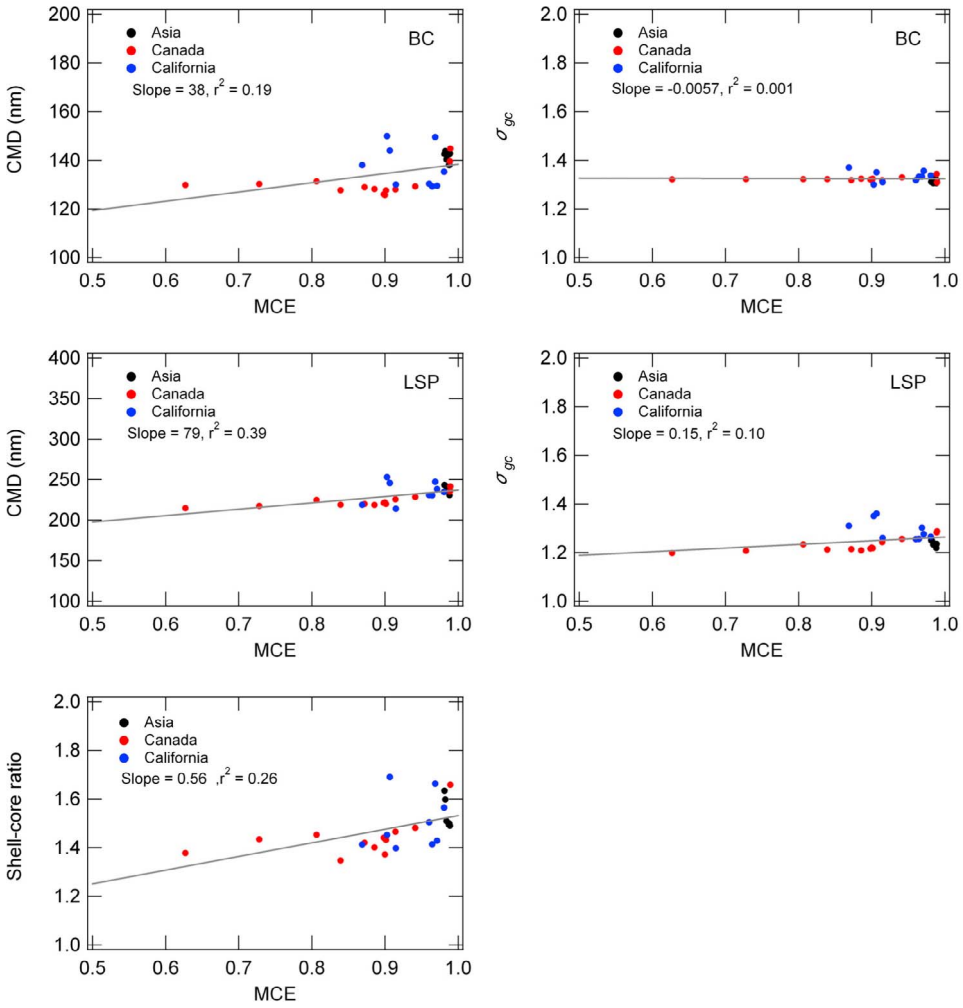

Figure 14. CMD and σ_g of (top) BC and (middle) LSP and (bottom) median shell/core ratios plotted versus MCE for the Asian and North American BB plumes. Linear regression fits using all the data points are also shown.

Figure 14 compares the average CMD and standard deviation (σ_{gc}) of BC and LSP and the median D_p/D_{BC} ratios in the North American and Asian plumes as a function of MCE. Table 7 summarizes the averages of the 1 σ values of the D_p/D_{BC} ratios together with the average D_p/D_{BC} ratios. The least squares fits were derived using the data sets with APT < 1 mm for Canada and California and APT < 5 mm for Asia. Some of the plumes in Canada were measured after 1–2 h after emissions, suggested from the NO_x/NO_y ratios (Table 4).

[75] As a whole, the CMD and σ_{gc} of BC did not change substantially without depending on the location of the fires, MCE, and age, although the CMD increased and σ_{gc} decreased slightly with the increase in MCE. The rate of growth BC by coagulation depends strongly on the initial BC concentration [e.g., *Hinds*, 1999; *Seinfeld and Pandis*, 2006]. After this initial growth, BC particles thickly coated by mainly organic compounds probably grew much more slowly by coagulation under largely diluted conditions. Coagulation generally increases the CMD and decreases σ_{gc} [*Kajino and Kondo*, 2011]. Figure 14 shows that the CMD and σ_{gc} of BC slightly increased and decreased, respectively, with the increase in MCE. The observed anticorrelation of CMD and σ_{gc} of BC is qualitatively consistent with this effect.

[76] The small variability of the size distributions of LSP measured by SP2 is also noteworthy, considering the differences in the vegetation and therefore different chemical compounds constituting the OA particles. The CMD and σ_{gc} increased slightly with the increase in MCE. These are the first extensive measurements of the size distributions of BC and LSP (mainly OA) emitted from boreal forest fires.

[77] The CMD and MMD of BC impacted by BB near the Gulf of Mexico were about 140 nm and 200 nm [*Schwarz et al.*, 2008], confirming the small variability of the size distributions of BC from BB. The ages of the BB plumes were estimated to be about 0.5–1.5 h. These observations simplify modeling efforts in expressing the size distributions of primary particles emitted from boreal forest fires. Namely, the BC and LSP number size distributions with ages older than a few hours are represented to a good approximation by lognormal distribution functions, with an average CMD = 138 nm and σ_g = 1.35 and an average CMD = 230 nm and σ_g = 1.32, respectively.

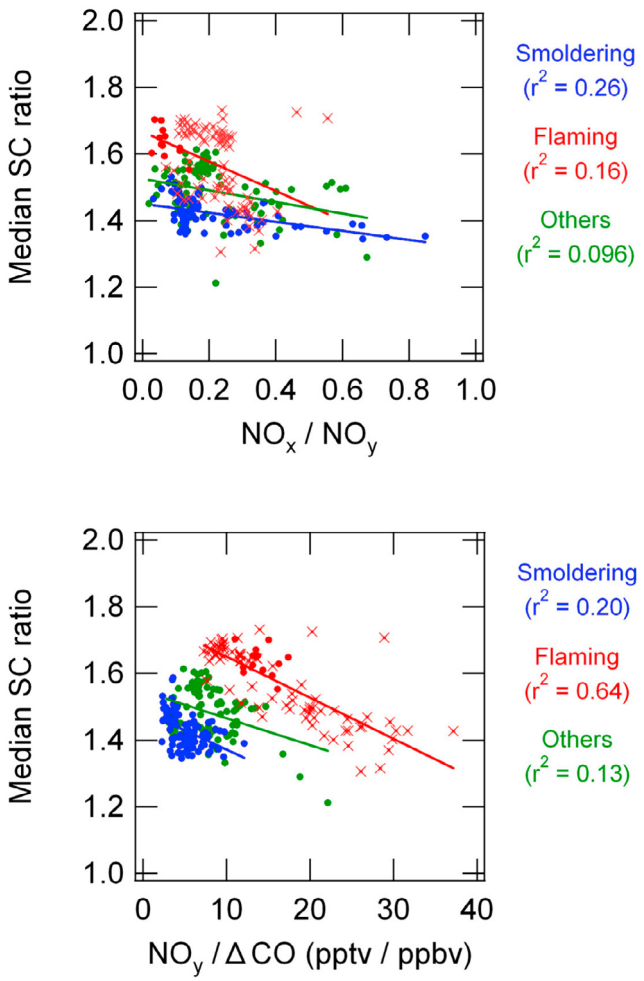

Figure 15. Median shell/core (SC) ratio plotted versus NO_x/NO_y and $NO_y/\Delta CO$ ratios in BB plumes during ARCTAS-B. The data points are color coded for the smoldering phase (MCE < 0.9; blue), flaming phase (MCE > 0.95: red), and others (0.90 < MCE < 0.95; green).

8.2. Evolution of the Mixing State of BC

8.2.1. Observed Features

[78] We investigated the evolution of the mixing state of BC for different phases of combustion mainly using the Canadian data, which contain data with largely different air mass ages. We used NO_x/NO_y and $NO_y/\Delta CO$ ratios as a measure of aging with different time scales. Figure 15 shows the median D_p/D_{BC} (SC) ratio versus the NO_x/NO_y and NO_y/CO ratios measured in the Canadian plumes. The data points are color coded with the phase of combustion. In the smoldering phase, the median D_p/D_{BC} ratio was ~1.35 for fresh plumes with NO_x/NO_y ~ 0.8. The average OH concentrations in the Canadian plumes were about $4 \pm 2 \times 10^6$ cm^{-3}. The ages of air masses with these NO_x/NO_y ratios are estimated to be 1–2 h considering oxidation of NO_x only by OH, neglecting the formation of PAN [*Kondo et al.*, 2008; *Alvarado et al.*, 2010]. This indicates that BC was thickly coated by organics 1–2 h after emission.

[79] For smoldering phase emissions, the D_p/D_{BC} ratio increased to 1.45 at NO_x/NO_y ratios of 0.05–0.1. The ages of plumes are roughly estimated to be about 12–24 h. The increase in the D_p/D_{BC} ratio from 1.35 to 1.45 corresponds to a 40 ± 30% increase of the volume of the coating materials. It should be noted that the estimate in the increase depends sensitively on the choice of the D_p/D_{BC} ratio. For the plumes with MCE between 0.9 and 0.95 (green points in Figure 15), the increase in volume can be as high as 80%, although the scatter is substantial.

[80] For the flaming phase plumes, we used the $NO_y/\Delta CO$ ratios as indicators of photochemical age, because these plumes were more aged than the smoldering plumes. The D_p/D_{BC} ratios clearly increased with the decrease in the NO_y/CO ratios shown in Figure 15 (bottom). The increase in the D_p/D_{BC} ratio from 1.4 at $NO_y/\Delta CO$ = 30 to 1.66 at $NO_y/\Delta CO$ = 10 corresponds to a 205 ± 40% increase of the volume of the coating materials.

[81] In very fresh BB plumes in Australia, the $NO_y/\Delta CO$ ratios were observed to increase with the increase with MCE [*Takegawa*, 2001]. They were about 40 pptv/ppbv and 20 pptv/ppbv at MCE = 0.96 and 0.92, respectively, similar to the present observations. NO_x emitted is converted to PAN and HNO_3, followed by conversion of PAN to HNO_3 and dry deposition of HNO_3 [e.g., *Mauzerall et al.*, 1998; *Takegawa et al.*, 2003; *Alvarado et al.*, 2010]. About 60% of NO_y was observed to decrease within 2–3 days [*Takegawa et al.*, 2003]. Most of the data shown in Figures 15 and 17 were obtained in the BL. The main conclusions discussed in this section are unchanged even if the BL data were selectively used.

[82] The changes in the NO_x/NO_y, PAN/NO_y, and HNO_3/NO_y ratios in the plumes in the flaming phase are shown in Figure 16, in order to understand the processes of the changes in the NO_y. It can be seen that about 70% of NO_x was lost by conversion to PAN and HNO_3 already at an $NO_y/\Delta CO$ ratio of 30 pptv/ppbv. The decrease in the $NO_y/\Delta CO$ ratios occurred mainly through the deposition of HNO_3, produced from NO_x. It is estimated that the increase in the D_p/D_{BC} ratios continued longer than about 2–3 days, considering the time scale of the NO_y loss, through HNO_3 deposition, as discussed above.

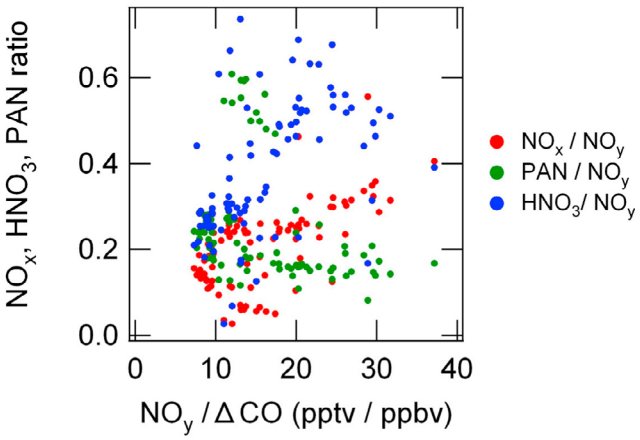

Figure 16. NO_x/NO_y, PAN/NO_y, and HNO_3/NO_y ratios versus $NO_y/\Delta CO$ ratios in the flaming phase plumes shown in Figure 15.

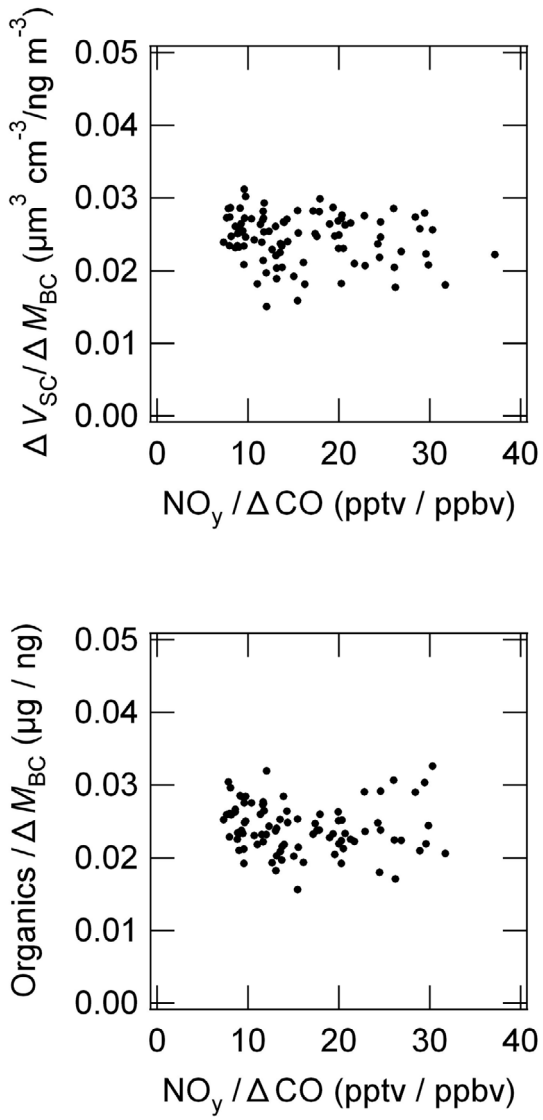

Figure 17. $\Delta V_{SC}/\Delta M_{BC}$ and OA/ΔM_{BC} ratios plotted versus the $NO_y/\Delta CO$ ratio in the flaming phase plumes shown in Figure 15.

[83] Figure 17 shows the $\Delta V_{SC}/\Delta M_{BC}$ and OA/ΔM_{BC} ratios versus the $NO_y/\Delta CO$ ratio. Figure 17 indicates no substantial increase in ΔV_{SC} and OA relative to ΔM_{BC} with age. Therefore it is unlikely that condensation of secondary aerosol species formed from precursor gases emitted directly from BB caused the increase in the D_p/D_{BC} ratios. Since the fraction of V_{SC} accounted for by the BC-containing particles is very small, a potential explanation for this apparent discrepancy is that OA was evaporating from particles that contained OA but not BC and then recondensing (possibly after gas phase oxidation) on the BC-containing particles in the SP2 size range [*Marcolli et al.*, 2004; *Robinson et al.*, 2007; *Grieshop et al.*, 2009].

8.2.2. Effect of Coagulation

[84] Brownian coagulation may also explain the observed evolution of the BC mixing state. Figure 18 shows the total number concentration of LSP particles (N_{sc}) versus the $NO_y/\Delta CO$ ratio. Generally N_{sc} was less than 3000 cm^{-3} and 1000 cm^{-3} in the BB plumes in smoldering and flaming phases, respectively. We use these data in calculating the effect of coagulation, as detailed below.

[85] A simple coagulation model was used to assess the effect of coagulation between LSP and BC on the evolution of the BC mixing state. The model solves for the intramodal coagulation and intermodal coagulation between the two modes, namely LSP (mode *i*) and BC (mode *j*). The evolution of number size distribution functions of LSP (n_i (v_{pi})) and BC (n_j (v_{pj})) due to intramodal coagulation can be expressed as [*Whitby and McMurry*, 1997],

$$\frac{d}{dt}n(v_p) = \frac{1}{2}\int_0^{v_p} \beta(\tilde{v}_p, v_p - \tilde{v}_p)n(\tilde{v}_p)n(v_p - \tilde{v}_p)d\tilde{v}_p - \int_0^{\infty} \beta(v_p, \tilde{v}_p)n(v_p)n(\tilde{v}_p)d\tilde{v}_p \quad (2)$$

where v_p and n (v_p) are the volume of a particle and number size distribution of mode *i* or *j*, respectively, and β is the Brownian coagulation kernel [*Binkowski and Shankar*, 1995]. Here $v_p = \pi D_p^3/6$, assuming that all particles are spherical. The evolutions of n_i (v_{pi}) and n_j (v_{pj}) due to intermodal coagulation are expressed as follows.

$$\frac{d}{dt}n_i(v_{pi}) = -\int_0^{\infty} \beta(v_{pi}, v_{pj})n_i(v_{pi})n_j(v_{pj})dv_{pj}$$

$$\frac{d}{dt}n_j(v_{pj}) = \int_0^{v_{pj}} \beta(v_{pi}, v_{pj} - v_{pi})n_i(v_{pi})n_j(v_{pj} - v_{pi})dv_{pi} - \int_0^{\infty} \beta(v_{pj}, v_{pi})n_j(v_{pj})n_i(v_{pi})dv_{pi} \quad (3)$$

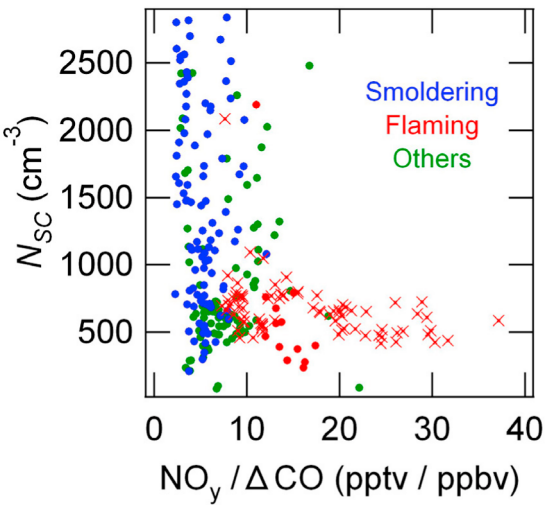

Figure 18. Total number concentrations of LSP particles plotted versus the $NO_y/\Delta CO$ ratios during ARCTAS-B for the smoldering phase (MCE < 0.9; blue), flaming phase (MCE > 0.95: red), and others (0.90 < MCE < 0.95; green).

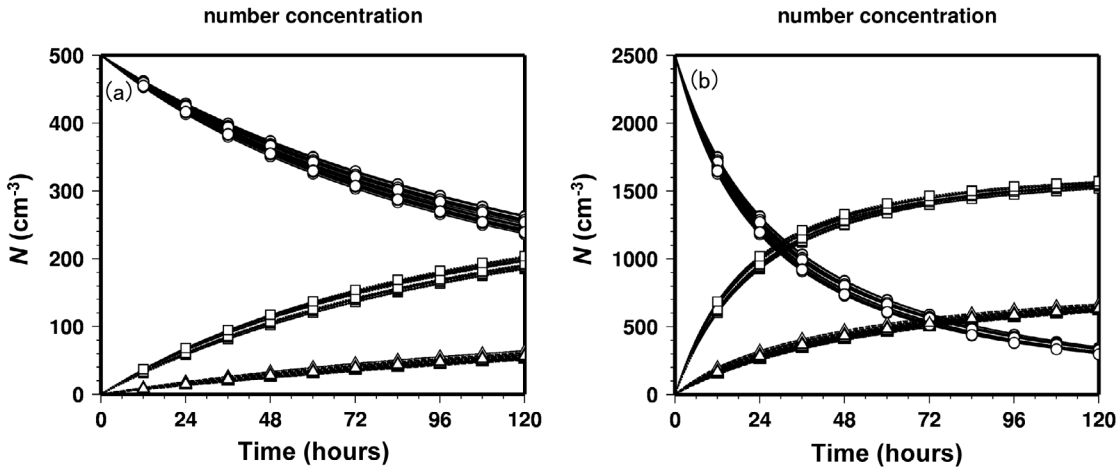

Figure 19. Total decay of N_{LSP} due to intramodal and intermodal coagulation, the decay due solely to intramodal coagulation (ΔN_{LSP} (intra)), and the decay due solely to intermodal coagulation (ΔN_{LSP} (inter)) for conditions of (a) N_{LSP} = 500 cm^{-3} and (b) N_{LSP} = 2500 cm^{-3}. ΔN_{LSP} (intra) and ΔN_{LSP} (inter) are shown as positive values. The other parameters for the initial lognormal size distribution (LNSD) are N_{LSP} = 500, 1500, and 2500 cm^{-3}; $N_{BC} = 0.1 \times N_{LSP}$; CMD_{LSP} = 200, 230, and 250 nm; CMD_{BC} (shell) = 120, 160, and 200 nm; σ_{LSP} = 1.2 and 1.4; and σ_{BC} = 1.2 and 1.3.

We assumed that the collision of a LSP particle (diameter of D_{pi}) with a BC particle (shell diameter of D_{pj}) forms a spherical BC particle with a shell diameter of $(D_{pi}^3 + D_{pj}^3)^{1/3}$, considering the conservation of volume concentration. Initially, n (v_p) was assumed have a lognormal size distribution (LNSD) function. The coagulation processes represented by equations (2) and (3) were calculated using the difference (bin) method, allowing deviations from the LNSD function.

[86] As initial conditions, the LNSD parameters were given covering the range of values shown in Figures 14 and 18. Namely, N_{SC} = 500, 1500, and 2500 cm^{-3}, $N_{BC} = 0.1 \times N_{LSP}$, CMD_{SC} = 200, 230, and 250 nm, CMD_{BC} (shell) = 120, 160, and 200 nm, σ_{SC} = 1.2 and 1.4, and σ_{BC} = 1.2 and 1.3. The detailed model settings are the same as BIN100 of *Kajino* [2011], in which the size distribution was divided into 100 bins between 1 nm and 1 μm, and 100 bins between 1 μm and 1 mm. The high accuracy of BIN100 is shown in his study.

[87] Figure 19 shows the total decay of N_{SC} due to intramodal and intermodal coagulation, the decay due solely to intramodal coagulation (ΔN_{SC} (intra)), and the decay due solely to intermodal coagulation (ΔN_{SC} (inter)) for N_{SC} = 500 cm^{-3} (Figure 19a) and N_{SC} = 2500 cm^{-3} (Figure 19b). ΔN_{SC} (intra) and ΔN_{SC} (inter) are shown as positive values. It can be seen that the decrease in N_{SC} is insensitive to the LNSD parameters, such as CMD and σ in the given range. In other words, the rates of coagulation are similar for the individual particles defined by these parameters. The rate of coagulation is higher at larger N_{SC}, as would be anticipated.

[88] The number of LSP colliding with BC particles in 1–2 days is nearly the same as the number of BC particles per unit volume of air. Namely, one BC particle collides with one LSP particle once in 1–2 days, on average. The collision of one BC and one LSP particle with similar sizes results in a 1.26 times (~$2^{1/3}$) increase in the SC ratio (D_p/D_{BC}). The SC ratio is predicted to increase from 1.2 to 1.5 by coagulation in 1–2 days. This result generally points out the importance of coagulation with LSP in increasing SC ratios with aging, in addition to condensation.

[89] Now we translate the results of Figure 19 into the changes of the volumes of shells coating BC cores. Figure 20 shows time series of the ratio of the total shell volume of BC at time t ($V(t) = \int v_p\, n(v_p, t)\, dv_p$) to the initial $V(t = 0)$ for some selected cases. The initial LNSD parameters are shown in Figure 20. Figure 20a is the result of calculations for conditions close to those for the observations. CMD_{BC} (shell) = 160 nm corresponds to a SC ratio of about 1.33 for CMD_{BC} (core) = 120 nm. The lines with triangles, squares, and circles are the results for initial CMD_{SC} = 250, 230, and 200 nm, respectively. Figure 20b is the same as Figure 20a but for CMD_{BC} (shell) = 120 nm (i.e., SC ratio = 1 for CMD_{BC} (core) = 120 nm). Figures 20c and 20d are the same as Figure 20a, but for an initial N_{SC} of 1500 and 2500 cm^{-3}. The increase in $V(t)$ is faster for larger CMD_{SC} in Figures 20a–20d.

[90] As discussed above, the rates of coagulation are insensitive to the parameters that define LNSD. Therefore, it is the difference in the size of LSP that contributes primarily to the difference in the rate of increase in the SC ratio or $V(t)$. Generally, larger σ_{SC} and larger differences between σ_{SC} and σ_{BC} result in faster increases in the SC ratio because of this mechanism. In fact, the rate of increase in SC is largest for σ_{SC} = 1.4 and σ_{BC} = 1.3 within the range of the parameters at the fixed CMDs. Therefore, the rates of changes in the SC ratio at σ_{SC} = 1.2 and σ_{BC} = 1.3 shown in Figure 20 are the lowest values.

[91] Figures 20a and 20b also show that the larger difference between CMD_{BC} and CMD_{SC} leads to the faster changes in the SC ratios for the same reason. The rate of the increase in the SC ratio is larger for higher number concentrations, as shown by the comparison of Figures 20a, 20c, and 20d. The $V(t)/V(0)$ ratio increases by factors of 1.5–3 (factors of 1.14–1.44 scaled for D_p/D_{BC}) in 1–2 days for the conditions

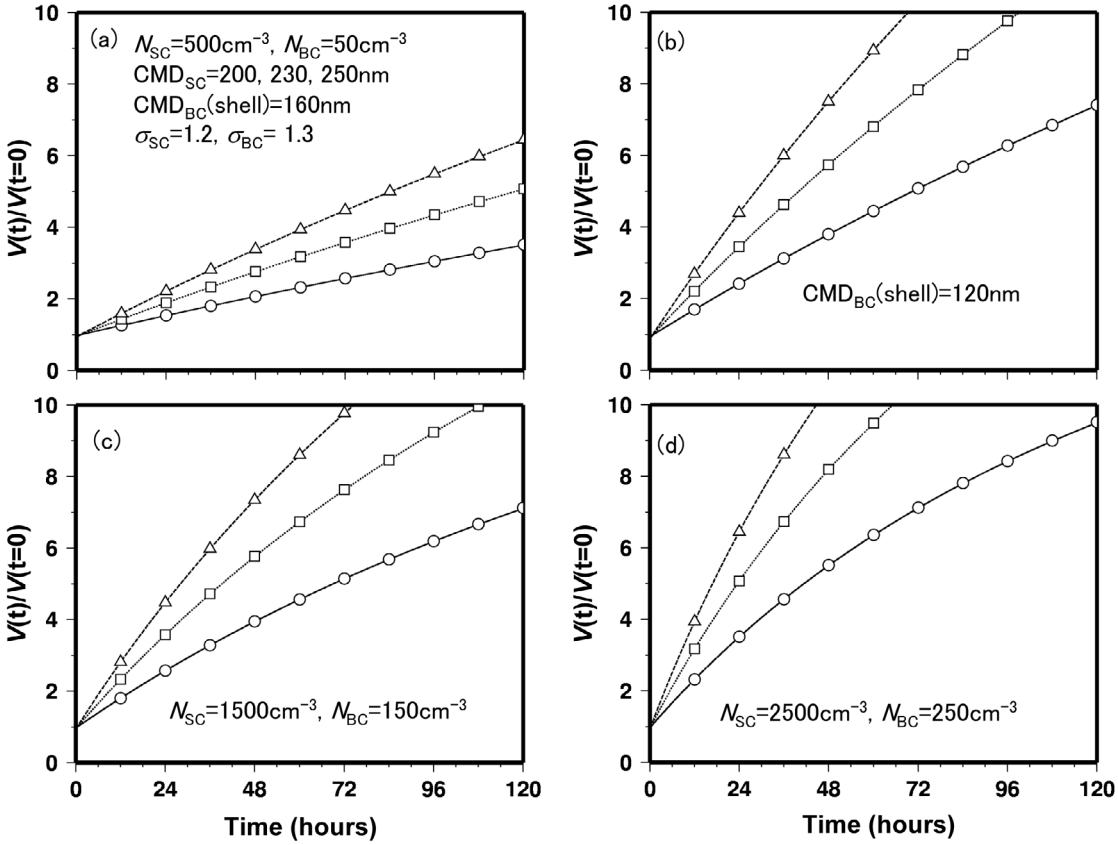

Figure 20. Time series of the ratios of the total shell volume of BC at time t ($V(t) = \int \pi [D_p(t)]^3 dD_p/6$) to the initial $V(t = 0)$ shown together with the initial LNSD parameters. (a) Calculations for the conditions of CMD_{BC} (shell) = 160 nm. The lines with triangles, squares, and circles are the results for initial CMD_{LSP} = 250, 230, and 200 nm, respectively. (b) Same as Figure 20a but for CMD_{BC} (shell) = 120 nm. (c and d) Same as Figure 20a but for initial N_{LSP} of 1500 and 2500 cm^{-3}, respectively.

of Figure 20a. This can largely explain the observed increase in D_p/D_{BC} ratio by a factor of about 1.2 in the flaming phase plumes.

[92] BC was thickly coated 1–2 h after emission, as discussed in section 8.2.1 (Figure 15). Near BB sources, N_{SC} can be substantially higher than 2500 cm^{-3}. In these areas, the coating of BC may occur in 1–2 h, considering the results shown in Figure 20d. Coagulation can play an important role in coating BC from early stages after BC emission from BB.

[93] Previous studies considered only condensation process to explain the evolution of the BC mixing state in plumes strongly impacted by anthropogenic emission [e.g., *Moteki et al.*, 2007; *Shiraiwa et al.*, 2007, 2008]. For the first time, we suggest that coagulation of LSP with BC can also effectively increase D_p/D_{BC} ratios based on the detailed comparison of observations and model calculations.

9. Conclusions

[94] We have presented multiple analyses of the ARCTAS chemical data combined with meteorological data to quantify the emissions (including secondary aerosol formation) of different types of aerosols (black carbon (BC) and organic and inorganic species) from biomass burning (BB) that occurred in North America (Canada and California) and Asia, especially in terms of modified combustion efficiency (MCE). The microphysical properties of aerosols (size distribution and mixing state) emitted from BB were also quantified. Data strongly impacted by BB were unambiguously extracted using tracers, namely CH_3CN and CH_2Cl_2. We also selected data with low accumulated precipitation along trajectory (APT) values to minimize the effect of wet removal of aerosol on the statistical analysis of the aerosol emissions from BB. Below, we summarize the most important parameters and processes presented above, which can be used directly for improving model estimates of the impact of BB in the Arctic.

[95] In North American plumes, organic aerosol (OA) constituted about 83% of the total PM_1, and the sulfate fraction was only 8% on average. By contrast, in the Asian plumes of the flaming phase, the sulfate fraction was as high as about 27%, with an OA fraction of about 60%, suggesting large SO_2 emissions from BB in Asia followed by oxidation during transport. In support of this interpretation, the sulfate + potential sulfate mass fractions were as high as 15%–20% in the BB plumes of the flaming phase in North America.

[96] In all types of BB plumes, the BC mass (volume) factions of the total PM_1(LSP) were 1%–5% (2%–4%), while the BC volume fractions were about 30% for the particles containing BC, consistent with the fact that most particles

did not contain BC. The $\Delta M_{BC}/\Delta V_{SC}$ ratios were much smaller than those for BC particles emitted from fossil fuel combustion.

[97] We derived the average emission ratios of M_{BC}/CO = 2.3 ± 2.2 ng m^{-3}/ppbv and M_{BC}/CO_2 = 180 ± 269 ng m^{-3}/ppmv for BB in North America. For BB plumes from Asia, the average ratios were M_{BC}/CO = 8.5 ± 5.4 ng m^{-3}/ppbv and M_{BC}/CO_2 = 129 ± 67 ng m^{-3}/ppmv. The much higher M_{BC}/CO ratios for the Asian plumes were likely due to higher MCE. The M_{BC}/CO ratios in North America were lower than the values compiled by *Andreae and Merlet* [2001] by a factor of 2–4, although the ratios for the Asian plumes were similar. The M_{BC}/CO_2 emission ratios for North America and Asia were 4–5 times lower than their estimates.

[98] We related the MCE to the emission ratios between ΔM_{BC}, ΔV_{SC}, ΔCO_2, and ΔCO for BB in North America and Asia. The $\Delta M_{BC}/\Delta CO_2$ ratios decreased with the increase in MCE, whereas the $\Delta M_{BC}/\Delta CO$ ratios increased with the increase in MCE. The dependence of the ratios on MCE is useful in improving emissions estimate of aerosols from BB and estimating the transport efficiency of aerosols by using tracers, especially CO.

[99] The shapes of the size distributions of BC were similar for plumes originating from BB in North America and Asia. The distribution functions were represented to a good approximation by lognormal functions. The count median diameters (CMDs) of BC were 136–141 nm (±6–8 nm), with standard deviations of 1.32–1.36 (±0.01–0.04) and little dependence on the phase of combustion.

[100] These BC particles were thickly coated by organics, with D_p/D_{BC} ratios of about 1.4 ($0.6 < MCE < 0.8$) 1–2 h after emission. In the smoldering phase, the D_p/D_{BC} ratios increased from 1.35 to 1.45 within about 12 h, with a corresponding increase in the volume of nonrefractory species on BC by 15%–40%. In aged flaming phase plumes, the increase in D_p/D_{BC} ratios continued for a few days, leading to an increase of the volume of coating materials by a factor of 2. A potential explanation is that OA was being redistributed via the gas phase [e.g., *Marcolli et al.*, 2004] by evaporating from particles that did not contain BC and recondensing on BC-containing particles.

[101] We assessed the effect of the Brownian coagulation of LSP with BC on the evolution of the BC mixing state. For the observed conditions, coagulation can increase D_p/D_{BC} ratios by factors of 1.2–1.5 in 1–2 days, depending on various parameters, influencing the rate of coagulation. Previous studies considered only condensation process to explain the evolution of the BC mixing state. For the first time, we suggest that coagulation of LSP with BC can effectively increase D_p/D_{BC} ratios, as well as condensation.

[102] **Acknowledgments.** The ARCTAS mission was supported by NASA. We are indebted to all the ARCTAS participants for their cooperation and support. Special thanks are due to the flight and ground crews of the NASA DC-8 aircraft. P. O. Wennberg provided the SO_2 data used for the present study. We thank M. Osuka for his assistance with the field measurements. R. Yokelson provided very useful comments on the manuscript. The meteorological data were supplied by the European Centre for Medium-Range Weather Forecasts (ECWMF). This work was supported in part by the Ministry of Education, Culture, Sports, Science, and Technology (MEXT); the Strategic International Cooperative Program of the Japan Science and Technology Agency (JST); and the Global Environment Research Fund of the Japanese Ministry of the Environment (B-083). Y.Z. was supported in part by the NASA Tropospheric Chemistry Program (USP-SMD-08-009). M.J.C. and J.L.J. acknowledge NASA grant NNX08D39G. CH_3CN measurements were supported by the Austrian Research Promotion Agency (FFG-ALR) and the Tiroler Zukunftstiftung, operated with the help and support of M. Graus, A. Hansel, and T. D. Maerk.

References

Adler, R. F., et al. (2003), The version 2 Global Precipitation Climatology Project (GPCP) monthly precipitation analysis (1979–present), *J. Hydrometeorol.*, *4*, 1147–1167, doi:10.1175/1525-7541(2003)004<1147:TVGPCP>2.0.CO;2.

Alvarado, M. J., et al. (2010), Nitrogen oxides and PAN in plumes from boreal fires during ARCTAS-B and their impact on ozone: An integrated analysis of aircraft and satellite observations, *Atmos. Chem. Phys.*, *10*, 9739–9760, doi:10.5194/acp-10-9739-2010.

Anderson, B. E., G. L. Gregory, J. E. Collins Jr., G. W. Sachse, T. J. Conway, and G. P. Whiting (1996), Airborne observations of spatial and temporal variability of tropospheric carbon dioxide, *J. Geophys. Res.*, *101*(D1), 1985–1997, doi:10.1029/95JD00413.

Andreae, M. O., and P. Merlet (2001), Emissions of trace gases and aerosols from biomass, *Global Biogeochem. Cycles*, *15*, 955–966, doi:10.1029/2000GB001382.

Binkowski, F. S., and U. Shankar (1995), The regional particulate matter model 1. Model description and preliminary results, *J. Geophys. Res.*, *100*(D12), 26,191–26,209, doi:10.1029/95JD02093.

Blake, N. J., et al. (2003), NMHCs and halocarbons in Asian continental outflow during the Transport and Chemical Evolution over the Pacific (TRACE-P) Field Campaign: Comparison with PEM-West B, *J. Geophys. Res.*, *108*(D20), 8806, doi:10.1029/2002JD003367.

Bohren, C. F., and D. R. Huffman (1998), *Absorption and Scattering of Light by Small Particles*, doi:10.1002/9783527618156, John Wiley, Hoboken, N. J.

Bowman, K. P. (2006), Transport of carbon monoxide from the tropics to the extratropics, *J. Geophys. Res.*, *111*, D02107, doi:10.1029/2005JD006137.

Brock, C. A., et al. (2008), Sources of particulate matter in the northeastern United States in summer: 2. Evolution of chemical and microphysical properties, *J. Geophys. Res.*, *113*, D08302, doi:10.1029/2007JD009241.

Brune, W. H., et al. (1999), OH and HO_2 chemistry in the North Atlantic free troposphere, *Geophys. Res. Lett.*, *26*, 3077–3080, doi:10.1029/1999GL900549.

Burling, I. R., et al. (2010), Laboratory measurements of trace gas emissions from biomass burning of fuel types from the southeastern and southwestern United States, *Atmos. Chem. Phys. Discuss.*, *10*, 16,425–16,473, doi:10.5194/acpd-10-16425-2010.

Chen, M., R. Talbot, H. Mao, B. Sive, J. Chen, and R. J. Griffin (2007), Air mass classification in coastal New England and its relationship to meteorological conditions, *J. Geophys. Res.*, *112*, D10S05, doi:10.1029/2006JD007687.

Choi, Y., S. Elliott, I. J. Simpson, D. R. Blake, J. J. Colman, M. K. Dubey, S. Meinardi, F. S. Rowland, T. Shirai, and F. A. Smith (2003), Survey of whole air data from the second airborne Biomass Burning and Lightning Experiment using principal component analysis, *J. Geophys. Res.*, *108*(D5), 4163, doi:10.1029/2002JD002841.

Christian, T. J., B. Kleiss, R. J. Yokelson, R. Holzinger, P. J. Crutzen, W. M. Hao, B. H. Saharjo, and D. E. Ward (2003), Comprehensive laboratory measurements of biomass-burning emissions: 1. Emissions from Indonesian, African, and other fuels, *J. Geophys. Res.*, *108*(D23), 4719, doi:10.1029/2003JD003704.

Clarke, A. D., and J. Noone (1985), Measurements of soot aerosol in Arctic snow, *Atmos. Environ.*, *19*, 2045–2053, doi:10.1016/0004-6981(85)90113-1.

Conard, S. G., A. I. Sukhinin, B. J. Stocks, D. R. Cahoon, E. P. Davidenko, and G. A. Ivanova (2002), Determining effects of area burned and fire severity on carbon cycling and emissions in Siberia, *Clim. Change*, *55*, 197–211, doi:10.1023/A:1020207710195.

Conny, J. M., and J. F. Slater (2002), Black carbon and organic carbon in aerosol particles from crown fires in the Canadian boreal forest, *J. Geophys. Res.*, *107*(D11), 4116, doi:10.1029/2001JD001528.

Crounse, J., et al. (2006), Measurement of gas-phase hydroperoxides by chemical ionization mass spectrometry, *Anal. Chem.*, *78*, 6726–6732, doi:10.1021/ac0604235.

Crounse, J., et al. (2009), Biomass burning and urban air pollution over the Central Mexican Plateau, *Atmos. Chem. Phys.*, *9*, 4929–4944, doi:10.5194/acp-9-4929-2009.

DeCarlo, P., J. G. Slowik, D. R. Worsnop, P. Davidvits, and J. L. Jimenez (2004), Particle morphology and density characterization by combined mobility and aerodynamic diameter measurements. Part 1: Theory, *Aerosol Sci. Technol.*, *38*, 1185–1205, doi:10.1080/027868290903907.

DeCarlo, P. F., et al. (2006), Field-deployable, high-resolution, time-of-flight aerosol mass spectrometer, *Anal. Chem.*, *78*, 8281–8289, doi:10.1021/ac061249n.

DeCarlo, P. F., et al. (2008), Fast airborne aerosol size and chemistry measurements above Mexico City and central Mexico during the MILAGRO campaign, *Atmos. Chem. Phys.*, *8*, 4027–4048, doi:10.5194/acp-8-4027-2008.

DeCarlo, P. F., et al. (2010), Investigation of the sources and processing of organic aerosol over the Central Mexican Plateau from aircraft measurements during MILAGRO, *Atmos. Chem. Phys.*, *10*, 5257–5280, doi:10.5194/acp-10-5257-2010.

de Gouw, J., and J. L. Jimenez (2009), Organic aerosols in the Earth's atmosphere, *Environ. Sci. Technol.*, *43*, 7614–7618, doi:10.1021/es9006004.

de Gouw, J. A., C. Warneke, D. D. Parrish, J. S. Holloway, M. Trainer, and F. C. Fehsenfeld (2003), Emission sources and ocean uptake of acetonitrile (CH_3CN) in the atmosphere, *J. Geophys. Res.*, *108*(D11), 4329, doi:10.1029/2002JD002897.

Delmas, R., J. P. Lacaux, and D. Brocard (1995), Determination of biomass burning emission factors: Method and results, *Environ. Monit. Assess.*, *38*, 181–204, doi:10.1007/BF00546762.

Drummond, J. R., and G. S. Mand (1996), The Measurements of Pollution in the Troposphere (MOPITT) instrument: Overall performance and calibration requirements, *J. Atmos. Oceanic Technol.*, *13*, 314–320, doi:10.1175/1520-0426(1996)013<0314:TMOPIT>2.0.CO;2.

Dunlea, E. J., et al. (2009), Evolution of Asian aerosols during transpacific transport in INTEX-B, *Atmos. Chem. Phys.*, *9*, 7257–7287, doi:10.5194/acp-9-7257-2009.

Eck, T. F., et al. (2009), Optical properties of boreal region biomass burning aerosols in central Alaska and seasonal variation of aerosol optical depth at an Arctic coastal site, *J. Geophys. Res.*, *114*, D11201, doi:10.1029/2008JD010870.

Ferek, R. J., J. S. Reid, P. V. Hobbs, D. R. Blake, and C. Liousse (1998), Emission factors of hydrocarbons, halocarbons, trace gases and particles from biomass burning in Brazil, *J. Geophys. Res.*, *103*(D24), 32,107–32,118, doi:10.1029/98JD00692.

Flanner, M. G., C. S. Zender, J. T. Randerson, and P. J. Rasch (2007), Present-day climate forcing and response from black carbon in snow, *J. Geophys. Res.*, *112*, D11202, doi:10.1029/2006JD008003.

Flanner, M. G., C. S. Zender, P. G. Hess, N. M. Mahowald, T. H. Painter, V. Ramanathan, and P. J. Rasch (2009), Springtime warming and reduced snow cover from carbonaceous particles, *Atmos. Chem. Phys.*, *9*, 2481–2497, doi:10.5194/acp-9-2481-2009.

Fors, E. O., et al. (2010), Hygroscopic properties of Amazonian biomass burning and European background HULIS and investigation of their effects on surface tension with two models linking H-TDMA to CCNC data, *Atmos. Chem. Phys.*, *10*, 5625–5639, doi:10.5194/acp-10-5625-2010.

Fuelberg, H. E., D. L. Harrigan, and W. Sessions (2010), A meteorological overview of the ARCTAS 2008 mission, *Atmos. Chem. Phys.*, *10*, 817–842, doi:10.5194/acp-10-817-2010.

Gao, R. S., J. P. Schwarz, K. K. Kelly, D. W. Fahey, L. A. Watts, and T. L. Thompson (2007), A novel method for estimating light-scattering properties of soot aerosols using a modified single-particle soot photometer, *Aerosol Sci. Technol.*, *41*, 125–135, doi:10.1080/02786820601118398.

Goode, J. G., R. J. Yokelson, D. E. Ward, R. A. Susott, R. E. Babbitt, M. A. Davies, and W. M. Hao (2000), Measurements of excess O_3, CO_2, CO, CH_4, C_2H_4, C_2H_2, HCN, NO, NH_3, HCOOH, CH_3COOH, HCHO, and CH_3OH in 1997 Alaskan biomass burning plumes by airborne Fourier transform infrared spectroscopy (AFTIR), *J. Geophys. Res.*, *105*, 22,147–22,166, doi:10.1029/2000JD900287.

Grieshop, A. P., J. M. Logue, N. M. Donahue, and A. L. Robinson (2009), Laboratory investigation of photochemical oxidation of organic aerosol from wood fires: Measurement and simulation of organic aerosol evolution, *Atmos. Chem. Phys.*, *9*, 1263–1277, doi:10.5194/acp-9-1263-2009.

Hallett, J., J. G. Hudson, and C. F. Rogers (1989), Characterization of combustion aerosols for haze and cloud formation, *Aerosol Sci. Technol.*, *10*, 70–83, doi:10.1080/02786828908959222.

Hansen, J., and L. Nazarenko (2004), Soot climate forcing via snow and ice albedos, *Proc. Natl. Acad. Sci. U. S. A.*, *101*, 423–428, doi:10.1073/pnas.2237157100.

Hinds, W. C. (1999), *Aerosol Technology*, 483 pp., John Wiley, New York.

Huffman, G. J., R. F. Adler, M. M. Morrissey, D. T. Bolvin, S. Curtis, R. Joyce, B. McGavock, and J. Susskind (2001), Global precipitation at one-degree daily resolution from multisatellite observations, *J. Hydrometeorol.*, *2*, 36–50, doi:10.1175/1525-7541(2001)002<0036:GPAODD>2.0.CO;2.

Jacob, D. J., et al. (2010), The Arctic Research of the Composition of the Troposphere from Aircraft and Satellite (ARCTAS) mission: Design, execution, and first results, *Atmos. Chem. Phys.*, *10*, 5191–5212, doi:10.5194/acp-10-5191-2010.

Jacobson, M. Z. (1999), Isolating nitrated and aromatic aerosols and nitrated aromatic gases as sources of ultraviolet light absorption, *J. Geophys. Res.*, *104*(D3), 3527–3542, doi:10.1029/1998JD100054.

Kajino, M. (2011), MADMS: Modal Aerosol Dynamics model for multiple Modes and fractal Shapes in the free-molecular and the near-continuum regimes, *J. Aerosol Sci.*, *42*, 224–248, doi:10.1016/j.jaerosci.2011.01.005.

Kajino, M., and Y. Kondo (2011), EMTACS: Development and regional-scale simulation of a size, chemical, mixing state and shape resolved atmospheric particle model, *J. Geophys. Res.*, *116*, D02303, doi:10.1029/2010JD015030.

Kim, H., B. Barkey, and S. E. Paulson (2010), Real refractive indices of α- and β-pinene and toluene secondary organic aerosols generated from ozonolysis and photo-oxidation, *J. Geophys. Res.*, *115*, D24212, doi:10.1029/2010JD014549.

Kim, S., et al. (2007), Measurement of pernitric acid in the free troposphere during the Intercontinental Chemical Transport Experiment–North America 2004, *J. Geophys. Res.*, *112*, D12S01, doi:10.1029/2006JD007676.

Koch, D., et al. (2009), Evaluation of black carbon estimations in global aerosol models, *Atmos. Chem. Phys.*, *9*, 9001–9026, doi:10.5194/acp-9-9001-2009.

Komhyr, W. D., R. H. Gammon, T. B. Harris, L. S. Waterman, T. J. Conway, W. R. Taylor, and K. W. Thoning (1985), Global atmospheric CO_2 distribution and variations from 1968–1982 NOAA/GMCC CO_2 flask sample data, *J. Geophys. Res.*, *90*(D3), 5567–5596, doi:10.1029/JD090iD03p05567.

Kondo, Y., et al. (2008), Formation and transport oxidized reactive nitrogen, ozone, and secondary organic aerosol in Tokyo, *J. Geophys. Res.*, *113*, D21310, doi:10.1029/2008JD010134.

Kondo, Y., et al. (2009), Stabilization of the mass absorption cross section of black carbon for filter-based absorption photometry by the use of a heated inlet, *Aerosol Sci. Technol.*, *43*, 741–756, doi:10.1080/02786820902889879.

Kondo, Y., et al. (2010), Formation and transport of aerosols in Tokyo in relation to their physical and chemical properties: A review, *J. Meteorol. Soc. Jpn.*, *88*, 597–624, doi:10.2151/jmsj.2010-401.

Kondo, Y., L. Sahu, N. Moteki, F. Khan, N. Takegawa, X. Liu, M. Koike, and T. Miyakawa (2011), Consistency and traceability of black carbon measurements made by laser-induced incandescence, thermal-optical transmittance, and filter-based photo-absorption techniques, *Aerosol Sci. Technol.*, *45*, 295–312, doi:10.1080/02786826.2010.533215.

Kuwata, M., Y. Kondo, and N. Takegawa (2009), Critical condensed mass for activation of black carbon as cloud condensation nuclei, *J. Geophys. Res.*, *114*, D20202, doi:10.1029/2009JD012086.

Lavoué, D., C. Liousse, H. Cachier, B. J. Stocks, and J. G. Goldammer (2000), Modeling of carbonaceous particles emitted by boreal and temperate wildfires at northern latitudes, *J. Geophys. Res.*, *105*, 26,871–26,890, doi:10.1029/2000JD900180.

Levin, E. J. T., et al. (2010), Biomass burning smoke aerosol properties measured during Fire Laboratory at Missoula Experiment (FLAME), *J. Geophys. Res.*, *115*, D18210, doi:10.1029/2009JD013601.

Lewis, K. A., et al. (2009), Reduction in biomass burning aerosol light absorption upon humidification: Roles of inorganically induced hygroscopicity, particle collapse, and photoacoustic heat and mass transfer, *Atmos. Chem. Phys.*, *9*, 8949–8966, doi:10.5194/acp-9-8949-2009.

Lubin, D., and A. M. Vogelmann (2006), A climatologically significant aerosol longwave indirect effect in the Arctic, *Nature*, *439*(7075), 453–456, doi:10.1038/nature04449.

Marcolli, C., B. P. Luo, T. Peter, and F. G. Wienhold (2004), Internal mixing of the organic aerosol by gas phase diffusion of semivolatile organic compounds, *Atmos. Chem. Phys.*, *4*, 2593–2599, doi:10.5194/acp-4-2593-2004.

Matsui, H., et al. (2011), Seasonal variation of the transport of black carbon aerosol from the Asian continent to the Arctic during the ARCTAS aircraft campaign, *J. Geophys. Res.*, *116*, D05202, doi:10.1029/2010JD015067.

Mauzerall, D. L., J. A. Logan, D. J. Jacob, B. E. Anderson, D. R. Blake, J. D. Bradshaw, B. Heikes, G. W. Sachse, H. Singh, and B. Talbot (1998), Photochemistry in biomass burning plumes and implications for tropospheric ozone over the tropical South Atlantic, *J. Geophys. Res.*, *103*, 8401–8423, doi:10.1029/97JD02612.

McNaughton, C. S., et al. (2007), Results from the DC-8 inlet characterization experiment (DICE): Airborne versus surface sampling of mineral dust and sea salt aerosols, *Aerosol Sci. Technol.*, *41*, 136–159, doi:10.1080/02786820601118406.

Moteki, N., and Y. Kondo (2007), Effects of mixing state on black carbon measurement by laser-induced incandescence, *Aerosol Sci. Technol.*, *41*, 398–417, doi:10.1080/02786820701199728.

Moteki, N., and Y. Kondo (2008), Method to measure time-dependent scattering cross sections of particles evaporating in a laser beam, *J. Aerosol Sci.*, *39*, 348–364.

Moteki, N., and Y. Kondo (2010), Dependence of laser-induced incandescence on physical properties of black carbon aerosols: Measurements and theoretical interpretation, *Aerosol Sci. Technol.*, *44*, 663–675, doi:10.1080/02786826.2010.484450.

Moteki, N., Y. Kondo, Y. Miyazaki, N. Takegawa, Y. Komazaki, G. Kurata, T. Shirai, D. R. Blake, T. Miyakawa, and M. Koike (2007), Evolution of mixing state of black carbon particles: Aircraft measurements over the western Pacific in March 2004, *Geophys. Res. Lett.*, *34*, L11803, doi:10.1029/2006GL028943.

Moteki, N., Y. Kondo, and S. Nakamura (2010), Method to measure refractive indices of small nonspherical particles: Application to black carbon particles, *J. Aerosol Sci.*, *41*, 513–521, doi:10.1016/j.jaerosci.2010.02.013.

Oshima, N., M. Koike, Y. Zhang, and Y. Kondo (2009), Aging of black carbon in outflow from anthropogenic sources using a mixing state resolved model: 2. Aerosol optical properties and condensation nuclei activities, *J. Geophys. Res.*, *114*, D18202, doi:10.1029/2008JD011681.

Park, K., D. B. Kittelson, M. R. Zachariah, and P. H. McMurry (2004), Measurement of inherent material density of nanoparticle agglomerates, *J. Nanopart. Res.*, *33*, 334–352.

Petters, M. D., and S. M. Kreidenweis (2007), A single parameter representation of hygroscopic growth and cloud condensation nucleus activity, *Atmos. Chem. Phys.*, *7*, 1961–1971, doi:10.5194/acp-7-1961-2007.

Reid, J. S., and P. V. Hobbs (1998), Physical and optical properties of young smoke from individual biomass fires in Brazil, *J. Geophys. Res.*, *103*(D24), 32,013–32,030, doi:10.1029/98JD00159.

Reid, J. S., R. Koppmann, T. F. Eck, and D. P. Eleuterio (2005), A review of biomass burning emissions part II: Intensive physical properties of biomass burning particles, *Atmos. Chem. Phys.*, *5*, 799–825, doi:10.5194/acp-5-799-2005.

Remer, L. A., et al. (2005), The MODIS aerosol algorithm, products, and validation, *J. Atmos. Sci.*, *62*, 947–973, doi:10.1175/JAS3385.1.

Riemer, N., H. Vogel, and B. Vogel (2004), Soot aging time scales in polluted regions during day and night, *Atmos. Chem. Phys.*, *4*, 1885–1893, doi:10.5194/acp-4-1885-2004.

Robinson, A. L., et al. (2007), Rethinking organic aerosols: Semivolatile emissions and photochemical aging, *Science*, *315*(5816), 1259–1262.

Sachse, G. W., G. F. Hill, L. O. Wade, and M. G. Perry (1987), Fast-response, high precision carbon monoxide sensor using a tunable diode laser absorption technique, *J. Geophys. Res.*, *92*, 2071–2081, doi:10.1029/JD092iD02p02071.

Schwarz, J. P., et al. (2006), Single-particle measurement of mid latitude black carbon and light-scattering aerosols from the boundary layer to the lower stratosphere, *J. Geophys. Res.*, *111*, D16207, doi:10.1029/2006JD007076.

Schwarz, J. P., et al. (2008), Measurement of the mixing state, mass, and optical size of individual black carbon particles in urban and biomass burning emissions, *Geophys. Res. Lett.*, *35*, L13810, doi:10.1029/2008GL033968.

Seinfeld, J. H., and S. N. Pandis (2006), *Atmospheric Chemistry and Physics*, 1203 pp., John Wiley, Hoboken, N. J.

Shiraiwa, M., Y. Kondo, N. Moteki, N. Takegawa, Y. Miyazaki, and D. R. Blake (2007), Evolution of mixing state of black carbon in polluted air from Tokyo, *Geophys. Res. Lett.*, *34*, L16803, doi:10.1029/2007GL029819.

Shiraiwa, M., Y. Kondo, N. Moteki, N. Takegawa, L. K. Sahu, A. Takami, S. Hatakeyama, S. Yonemura, and D. R. Blake (2008), Radiative impact of mixing state of black carbon aerosol in Asian outflow, *J. Geophys. Res.*, *111*, D24210, doi:10.1029/2008JD010546.

Shiraiwa, M., Y. Kondo, T. Iwamoto, and K. Kita (2010), Amplification of light absorption of black carbon by organic coating, *Aerosol Sci. Technol.*, *44*, 46–54, doi:10.1080/02786820903357686.

Singh, H. B., et al. (2010), Pollution influences on atmospheric composition and chemistry at high northern latitudes: Boreal and California forest fire emissions, *Atmos. Environ.*, *44*, 4553–4564, doi:10.1016/j.atmosenv.2010.08.026.

Skamarock, W. C., et al. (2008), A description of the Advanced Research WRF version 3, *NCAR Tech. Note, NCAR/TN-475+STR*, 113 pp., Natl. Cent. for Atmos. Res., Boulder, Colo.

Slusher, D. L., L. G. Huey, D. L. Tanner, F. M. Flocke, and J. M. Roberts (2004), A thermal dissociation-chemical ionization mass spectrometry (TD-CIMS) technique for the simultaneous measurement of peroxyacyl nitrates and dinitrogen pentoxide, *J. Geophys. Res.*, *109*, D19315, doi:10.1029/2004JD004670.

Soja, A. J., W. R. Cofer, H. H. Shugart, A. I. Sukhinin, P. W. Stackhouse Jr., D. J. McRae, and S. D. Conard (2004), Estimating fire emissions and disparities in boreal Siberia (1998–2002), *J. Geophys. Res.*, *109*, D14S06, doi:10.1029/2004JD004570.

Stier, P., J. H. Seinfeld, S. Kinne, J. Feichter, and O. Boucher (2006), Impact of nonabsorbing anthropogenic aerosols on clear-sky atmospheric absorption, *J. Geophys. Res.*, *111*, D18201, doi:10.1029/2006JD007147.

Stocks, B. J., et al. (1998), Climate change and forest fire potential in Russian and Canadian boreal forests, *Clim. Change*, *38*, 1–13, doi:10.1023/A:1005306001055.

Stocks, B. J., et al. (2002), Large forest fires in Canada, 1959–1997, *J. Geophys. Res.*, *107*, 8149, doi:10.1029/2001JD000484. [Printed *108*(D1), 2003.]

Stohl, A., et al. (2005), Technical note: The Lagrangian particle dispersion model FLEXPART version 6.2, *Atmos. Chem. Phys.*, *5*, 2461–2474, doi:10.5194/acp-5-2461-2005.

Stohl, A., et al. (2006), Pan-Arctic enhancements of light absorbing aerosol concentrations due to North American boreal forest fires during summer 2004, *J. Geophys. Res.*, *111*, D22214, doi:10.1029/2006JD007216.

Stohl, A., et al. (2007), Arctic smoke—Record high air pollution levels in the European Arctic due to agricultural fires in eastern Europe in spring 2006, *Atmos. Chem. Phys.*, *7*(2), 511–534, doi:10.5194/acp-7-511-2007.

Takegawa, N. (2001), Effects of biomass burning on atmospheric chemistry over Australia, Ph.D. thesis, Univ. of Tokyo, Tokyo.

Takegawa, N., et al. (2003), Removal of NO_x and NO_y in biomass burning plumes in the boundary layer over northern Australia, *J. Geophys. Res.*, *108*(D10), 4308, doi:10.1029/2002JD002505.

Takegawa, N., et al. (2004), Removal of NO_x and NO_y in Asian outflow plumes: Aircraft measurements over the western Pacific in January 2002, *J. Geophys. Res.*, *109*, D23S04, doi:10.1029/2004JD004866.

Takegawa, N., T. Miyakawa, Y. Kondo, J. L. Jimenez, D. R. Worsnop, and M. Fukuda (2006), Seasonal and diurnal variations of submicron organic aerosol in Tokyo observed using the Aerodyne Aerosol Mass Spectrometer, *J. Geophys. Res.*, *111*, D11206, doi:10.1029/2005JD006515.

Tans, P. P., T. J. Conway, and T. Nakazawa (1989), Latitudinal distribution of the sources and sinks of atmospheric carbon dioxide derived from surface observations and an atmospheric transport model, *J. Geophys. Res.*, *94*(D4), 5151–5172, doi:10.1029/JD094iD04p05151.

Textor, C., et al. (2006), Analysis and quantification of the diversities of aerosol life cycles within AeroCom, *Atmos. Chem. Phys.*, *6*, 1777–1813, doi:10.5194/acp-6-1777-2006.

Treffeisen, R., et al. (2007), Arctic smoke—Aerosol characteristics during a record smoke event in the European Arctic and its radiative impact, *Atmos. Chem. Phys.*, *7*(11), 3035–3053, doi:10.5194/acp-7-3035-2007.

Vay, S. A., et al. (2003), Influence of regional-scale anthropogenic emissions on CO_2 distributions over the western North Pacific, *J. Geophys. Res.*, *108*(D20), 8801, doi:10.1029/2002JD003094.

Vestin, A., J. Rissler, E. Swietlicki, G. P. Frank, and M. O. Andreae (2007), Cloud-nucleating properties of the Amazonian biomass burning aerosol: Cloud condensation nuclei measurements and modeling, *J. Geophys. Res.*, *112*, D14201, doi:10.1029/2006JD008104.

Ward, D. E., A. Setzer, Y. J. Kaufman, and R. A. Rasmussen (1991), Characteristics of smoke emissions from biomass fires of the Amazon region-Base-A experiment, in *Global Biomass Burning*, edited by J. S. Levine, pp. 394–402, MIT Press, Cambridge, Mass.

Warneke, C., et al. (2009), Biomass burning in Siberia and Kazakhstan as an important source for haze over Alaskan Arctic in April 2008, *Geophys. Res. Lett.*, *36*, L02813, doi:10.1029/2008GL036194.

Warneke, C., et al. (2010), An important contribution to springtime Arctic aerosol from biomass burning in Russia, *Geophys. Res. Lett.*, *37*, L01801, doi:10.1029/2009GL041816.

Warren, S. G., and W. J. Wiscombe (1980), A model for the spectral albedo of snow. II: Snow containing atmospheric aerosol, *J. Atmos. Sci.*, *37*, 2734–2745, doi:10.1175/1520-0469(1980)037<2734:AMFTSA>2.0.CO;2.

Weinheimer, A. J., J. G. Walega, B. A. Ridley, B. L. Gary, D. R. Blake, N. J. Blake, F. S. Rowland, G. W. Sachse, B. E. Anderson, and J. E. Collins (1994), Meridional distributions of NO_x, NO_y, and other species in the lower stratosphere and upper troposphere during AASE II, *Geophys. Res. Lett.*, *21*, 2583–2586, doi:10.1029/94GL01897.

Whitby, E. R., and P. H. McMurry (1997), Modal aerosol dynamics modeling, *Aerosol Sci. Technol.*, *27*(6), 673–688, doi:10.1080/02786829708965504.

Wisthaler, A., A. Hansel, R. R. Dickerson, and P. J. Crutzen (2002), Organic trace gas measurements by PTR-MS during INDOEX 1999, *J. Geophys. Res.*, *107*(D19), 8024, doi:10.1029/2001JD000576.

Yokelson, R. J., D. W. T. Griffith, and D. E. Ward (1996), Open-path Fourier transform infrared studies of large-scale laboratory biomass fires, *J. Geophys. Res.*, *101*(D15), 21,067–21,080, doi:10.1029/96JD01800.

Yokelson, R. J., J. G. Goode, D. E. Ward, R. A. Susott, R. E. Babbitt, D. D. Wade, I. Bertschi, D. W. T. Griffith, and W. M. Hao (1999), Emissions of formaldehyde, acetic acid, methanol, and other trace gases from bio-

mass fires in North Carolina measured by airborne Fourier transform infrared spectroscopy, *J. Geophys. Res.*, *104*, 30,109–30,125, doi:10.1029/1999JD900817.

Yokelson, R., et al. (2007), Emissions from forest fires near Mexico City, *Atmos. Chem. Phys.*, *7*, 5569–5584, doi:10.5194/acp-7-5569-2007.

Yokelson, R. J., T. J. Christian, T. G. Karl, and A. Guenther (2008), The tropical forest and fire emissions experiment: Laboratory fire measurements and synthesis of campaign data, *Atmos. Chem. Phys.*, *8*, 3509–3527, doi:10.5194/acp-8-3509-2008.

Yokelson, R. J., et al. (2009), Emissions from biomass burning in the Yucatan, *Atmos. Chem. Phys.*, *9*, 5785–5812, doi:10.5194/acp-9-5785-2009.

B. Anderson, G. S. Diskin, and S. Vay, NASA Langley Research Center, Hampton, VA 23681, USA. (b.e.anderson@larc.nasa.gov; glenn.s.diskin@nasa.gov; stephanie.a.vay@nasa.gov)

D. R. Blake, Department of Chemistry, University of California, Irvine, CA 92697-2025, USA. (drblake@uci.edu)

W. H. Brune, Department of Meteorology, Pennsylvania State University, University Park, PA 16802, USA. (brune@meteo.psu.edu)

M. J. Cubison and J. L. Jimenez, Department of Chemistry and Biochemistry, University of Colorado at Boulder, Boulder, CO 80309-0216, USA. (michael.cubison@colorado.edu; jose.jimenez@colorado.edu)

H. Fuelberg, Department of Meteorology, Florida State University, Tallahassee, FL 32306-3034, USA. (fuelberg@met.fsu.edu)

L. G. Huey, School of Earth and Atmospheric Sciences, Georgia Institute of Technology, 221 Bobby Dodd Way, Atlanta, GA 30332-0340, USA. (greg.huey@eas.gatech.edu)

M. Kajino, Meteorological Research Institute, 1-1 Nagamine, Tsukuba, Ibaraki 305-0052, Japan. (kajino@mri-jma.go.jp)

D. J. Knapp and A. J. Weinheimer, Atmospheric Chemistry Division, National Center for Atmospheric Research, 1850 Table Mesa Dr., Boulder, CO 80305, USA. (david@ucar.edu; wein@ucar.edu)

Y. Kondo, H. Matsui, N. Moteki, and N. Takegawa, Research Center for Advanced Science and Technology, University of Tokyo, 4-6-1 Komaba, Meguro-ku, Tokyo 153-8904, Japan. (y.kondo@atmos.rcast.u-tokyo.ac.jp; matsui@atmos.rcast.u-tokyo.ac.jp; moteki@atmos.rcast.u-tokyo.ac.jp; takegawa@atmos.rcast.u-tokyo.ac.jp)

T. Mikoviny and A. Wisthaler, Institute of Ion Physics and Applied Physics, University of Innsbruck, Technikerstr. 25, A-6020 Innsbruck, Austria. (tomas.mikoviny@uibk.ac.at; armin.wisthaler@uibk.ac.at)

L. Sahu, Physical Research Laboratory, Ahmedabad 380009, India. (lokesh@prl.res.in)

Y. Zhao, Air Quality Research Center, University of California, One Shields Ave., Davis, CA 95616, USA. (yjzhao@ucdavis.edu)